Simultaneous photocatalytic removal of Cr (VI) and 4-Nitrophenol using CuNiFe LDH/Carbon nitride nanosheets under Visible Light

By

Fariah Salam

Registration No. 02312113001

Department of Environmental Sciences

Faculty of Biological Sciences

Quaid-i-Azam University

Islamabad, Pakistan

2021-2023

Simultaneous photocatalytic removal of Cr (VI) and 4-Nitrophenol using CuNiFe LDH/Carbon nitride nanosheets under Visible Light

This work is submitted in partial fulfillment for the award of the degree of

Master of Philosophy

in

Environmental Sciences

By

Fariah Salam

Registration No. 02312113001

Department of Environmental Sciences

Faculty of Biological Sciences

Quaid-i-Azam University

Islamabad, Pakistan

2023

To my Family for their faith, endless love, support, and encouragement

Certificate of Approval

This is hereby certified that the research work presented in this thesis, entitled "**Simultaneous Photocatalytic Removal of Cr (VI) and 4-Nitrophenol using CuNiFe LDH/Carbon Nitride Nanosheets under Visible Light**," was conducted by Fariah Salam (**Reg. No. 02312113001**) under the supervision of Dr. Abdullah Khan. No part of this thesis has been submitted elsewhere for any other degree. This thesis is submitted to the Department of Environmental Sciences in partial fulfillment of the requirements for the degree of Master of Philosophy in the field of Environmental Science at Quaid-i-Azam University, Islamabad, Pakistan.

Fariah Salam

Supervisor:

Dr. Muhammad Abdullah Khan

Associate Professor
Department of Environmental Sciences
Quaid-i-Azam University, Islamabad.

Chairperson:
Dr. Abida Farooqi
Associate Professor
Department of Environmental Sciences
Quaid-i-Azam University, Islamabad.
Date.

Author's Declaration

I, **Fariah Salam (Registration No. 02312113001)**, hereby affirm that my M.Phil. thesis titled "**Simultaneous Photocatalytic Removal of Cr (VI) and 4-Nitrophenol using CuNiFe LDH/Carbon Nitride Nanosheets under Visible Light**," was conducted by me in the Renewable Advancement Laboratory, Department of Environmental Sciences, Quaid-i-Azam University, Islamabad. The results, findings, conclusions, and investigations of this research have not been previously presented or published as research work in any other university.

Fariah Salam

Registration No. 02312113001

Plagiarism Undertaking

I, **Fariah Salam**, solemnly declare that my M.Phil. thesis titled **"Simultaneous Photocatalytic Removal of Cr (VI) and 4-Nitrophenol using CuNiFe LDH/Carbon Nitride Nanosheets under Visible Light"** represents solely my research work, with no significant contribution from any other person. Any small contributions or assistance received have been duly acknowledged, and the entire thesis has been composed by me.

I am fully aware of the zero-tolerance policy of the Higher Education Commission (HEC) and Quaid-i-Azam University, Islamabad, towards plagiarism. As the author of this thesis, I assert that no portion of my work has been plagiarized, and any material used as a reference is appropriately referred to and cited.

I acknowledge that, if I am found guilty of any form of plagiarism in the stated thesis, even after the award of my M.Phil. degree, the university reserves the right to withdraw or revoke my M.Phil. degree. Additionally, both the HEC and the university retain the right to publish my name on their respective websites, where the names of students who have committed plagiarism are listed.

Fariah Salam

ACKNOWLEDGMENT

I humbly express my gratitude to ALLAH ALMIGHTY, whose infinite kindness and mercy have blessed me with the most understanding and supportive parents, teachers, and friends. They serve as the source of my aspirations and motivations, providing me with the ability and strength to conduct the present research.

I extend my sincere thanks to my supervisor, Dr. Muhammad Abdullah Khan, at Quaid-i-Azam University, for his guidance and governance. His insights and expertise have been invaluable in assisting my research.

I would like to acknowledge my senior lab fellows for their step-by-step guidance, which contributed significantly to my learning process. Special thanks go to my fellow researchers, Tahira Nadir, and Nimra Zafar Cheema, for their support. I also express my gratitude to our lab assistant, Mr. Ayub Khasana, for his tireless services.

Lastly, I want to express my deepest appreciation to my parent and siblings for their unwavering support and encouragement throughout my entire life. Finally, I commend myself for undertaking something I have never done before.

Thank you all.

Fariah Salam

ABBREVIATIONS

WWTP	Wastewater Treatment Plant
4-NP	4-Nitrophenol
2-CP	2-chlorophenol
LEV	Levofloxacin
Cr(VI)	Hexavalent Chromium
VB	Valence Band
CB	Conduction Band
C_3N_4	Graphitic carbon nitride
CuNiFe	Copper Nickle Iron
LDH	Layered Double Hydroxide
DPC	1, 5 Diphenyl carbazide
ε_g	Band Gap
AOP	Advanced Oxidation Process
e^--h	Electron-Hole
PL	Photoluminescence
XRD	X-ray Diffraction
SEM	Scanning Electron Microscope
UV-Vis	Ultraviolet-Visible
LMCT	Ligand Metal Charge Transfer
DRS	Diffuse Reflectance Spectroscopy
FTIR	Fourier Transform Infrared

LIST OF FIGURES

LIST OF TABLES

TABLE OF CONTENT

HIGHLIGHTS

1. A photoactive CuNiFe LDH/C_3N_4 composite catalyst was prepared to investigate the behaviour of organics and Cr(VI) in a simultaneous system.

2. The optimized composite 1:2 (CuNiFe LDH/C_3N_4) exhibited improved charge separation, attributed to the layered structure and the transition metal charge transfer in CuNiFe LDH.

3. Study unravels that chemical nature of the organics affects the Cr(VI) reduction in simultaneous photocatalytic operation.

4. Reusability studies demonstrated that CuNiFe LDH/C_3N_4 maintained stability over four runs.

GRAPHICAL ABSTRACT

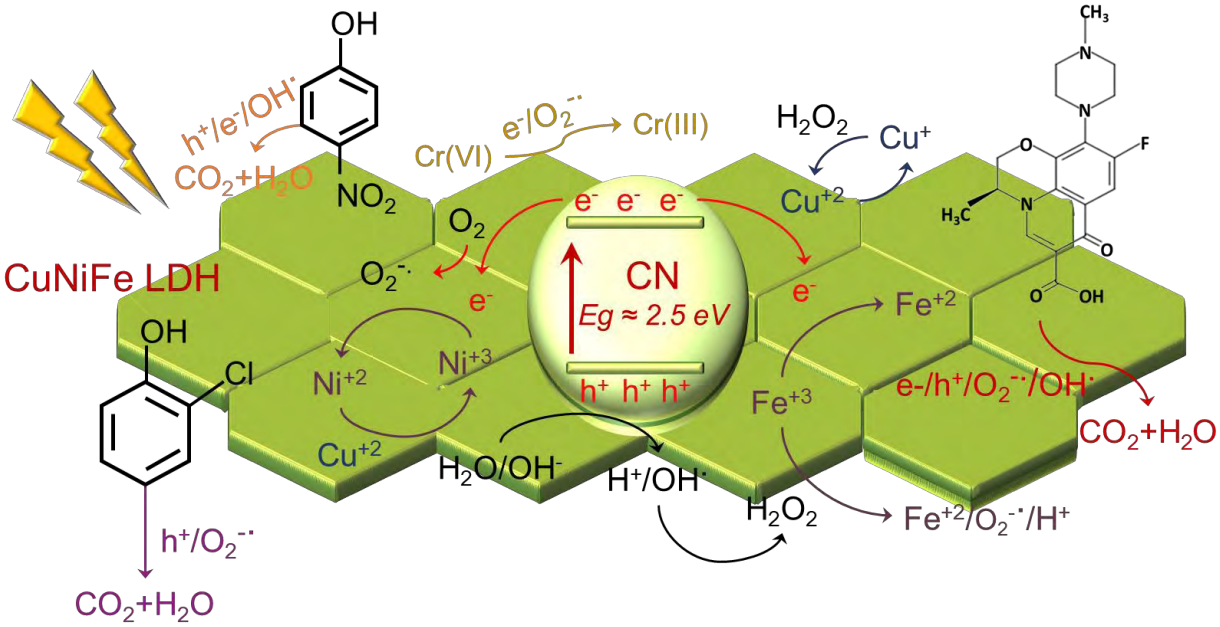

The presence of organics affects the photoreduction of Cr(VI) in simultaneous photocatalytic system.

ABSTRACT

Photocatalysis has made significant progress in the treatment of wastewater. Photocatalytic systems are constantly improving to incorporate the complexity of real environmental matrices, so that the results can be implemented for practical use. As the host of pollutants (organics and heavy metals) coexist in wastewater, it is important to understand how their presence influences remediation interventions. This study investigates simultaneous degradation of different organics and reduction of heavy metals in a concurrent photocatalytic reaction. A new CuNiFe LDH/C_3N_4 composite catalyst was synthesized to examine the photoredox behavior of different organics (4-nitophenol, 2-chlorophenol and levofloxacin) in presence of Cr(VI). The system was thoroughly characterized using a variety of structural, morphological, and optical techniques (such as XRD, SEM, FTIR, UV-Vis, and PL). CuNiFe LDH/C_3N_4 photocatalyst demonstrates enhanced charged transfer due to highly dispersed MO_6 in brucite-like sheets, and transition metals electron transfer. First, a 62.5% of Cr(VI) reduction was achieved in 180 minutes which increases to 72% and 78% in the presence of 4-NP and LEV, respectively. However, reduction decreases to 41% with 2-CP. Additionally, 4-NP, 2-CP, and LEV show a photocatalytic degradation of 59.15%, 57.9%, and 63.1%, respectively, when treated alone. Intriguingly, in the presence of Cr(VI), the degradation of 4-NP decreases to 19%, while the degradation of 2-CP (88.4%) and LEV (68%) remain significantly higher. Furthermore, radical scavenging experiments were performed to assess the species involved in the removal of the targeted pollutants. Based on these results, a generalized mechanism for this photoredox process was proposed. The work is a step forward in implementing photocatalytic systems for the remediation of complex environmental matrices.

1. INTRODUCTION

Pollution is an intricately complex phenomenon with profound impacts on ecosystem health. This complexity arises from diverse sources like transport industries, residential areas, and mining activities, releasing a variety of pollutants such as organic and inorganic substances, radioactive materials, and pathogens [1]. The challenge is further heightened by the dynamic movement of these pollutants across different environmental matrices. Moreover, the interaction of mixed pollutants adds another layer of intricacy, making it difficult to predict their cumulative impact. This intricate nature of pollution has adverse effects on human lives, economies, soil, and water salinity, disrupting the delicate balance of the food chain [2]. Wastewater treatment plants (WWTPs) encounter difficulties in treating specific pollutants. As a result, sludge from WWTPs and leachate and runoff from landfills may infiltrate groundwater and surface water. This issue is compounded by the application of biosolids or sewage sludge on land for soil nourishment, introducing highly soluble pollutants into the environment.

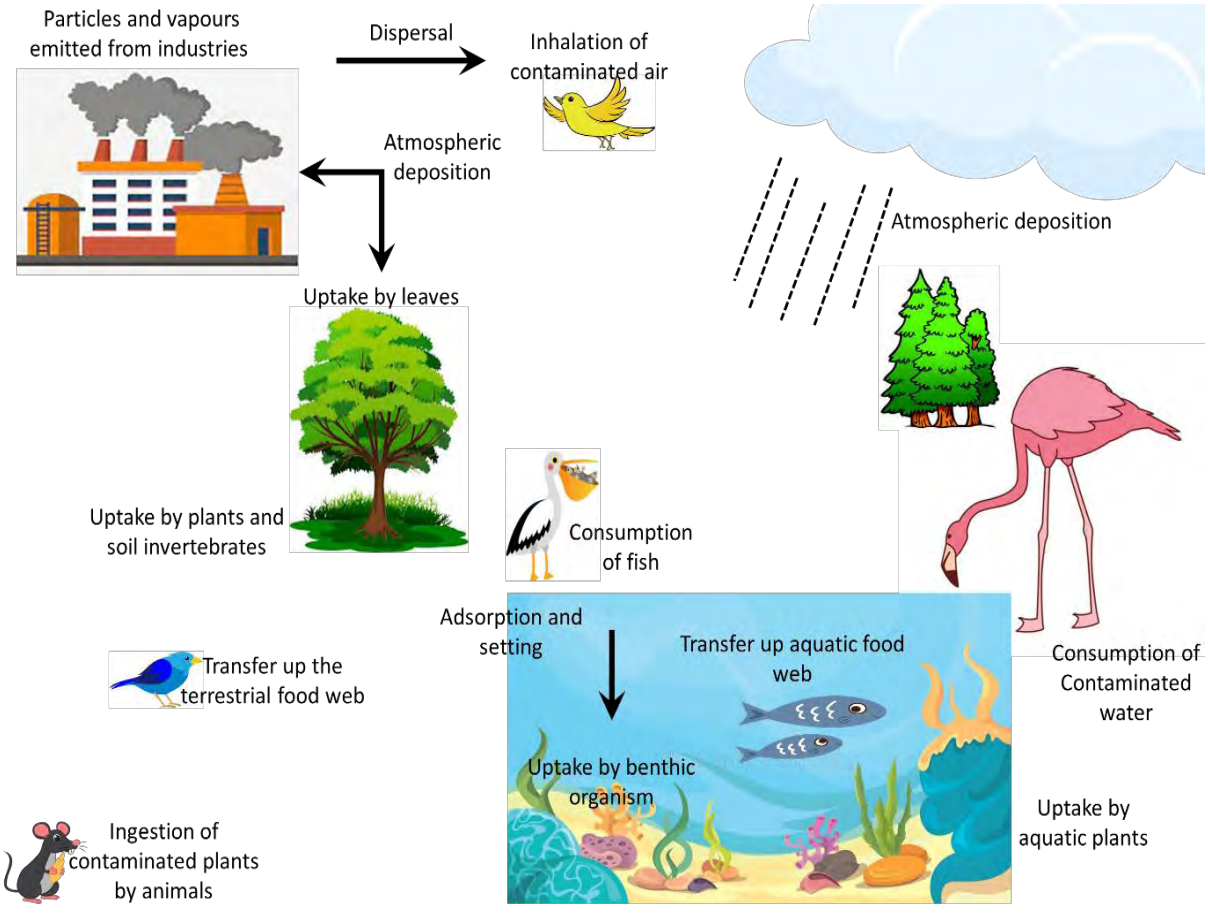

Figure 1.1: Fate and transport of pollutants in the environment [2].

1.1 Co-existence of pollutants in water

Improper disposal of wastewater and inadequate waste management practices in various industries contributes to the co-existence of various organic and inorganic pollutants Around 30% of the inorganic impurities present in sewage wastewater are comprised of heavy metals. The concurrent presence of heavy metals and organic substances in surface and ground water arises from their extensive use in various industrial activities, including tannery, distillery, paper, and dye industries, leading to pollution in aquatic environments [3]. Furthermore, aquatic ecosystems demonstrate the existence of heavy metals such as cadmium, mercury, copper, zinc, nickel, cobalt, and chromium, originating from petrochemical industries, mining operations, electroplating, and pharmaceutical activities [4]. The diverse structures and properties of these pollutants pose a significant challenge for complete decontamination, even with traditional methods.

The presence of a combination of heavy metals and pharmaceuticals in water environments and their potential impact on human and animal health is a matter of concern. In Chengdu, China, wastewater sources revealed ofloxacin and roxithromycin as the most prevalent antibiotics, while manganese (Mn), iron (Fe), zinc (Zn), copper (Cu), chromium (Cr), arsenic (As), palladium (Pd), and cadmium (Cd) were identified among the detected heavy metals [5]. Similarly, in the Rawat Industrial Zone, Pakistan, pharmaceutical wastewater contained heavy metals such as chromium (Cr), cadmium (Cd), lead (Pb), nickel (Ni), iron (Fe), and zinc (Zn) [6]. The existence of heavy metals and phenolic compounds poses a threat to living organisms. Along the coastal area in Karachi, surface water was reported to contain heavy metals like nickel (Ni), iron (Fe), and chromium (Cr), along with phenolic compounds exceeding permissible discharge limits into the sea [7]. The discharge of waste from petrochemical and coal industries, leather processing, electroplating, paper-making, dyeing, aquaculture, and metallurgy significantly contributes to the substantial volume of wastewater entering surface waters [8]. Research focusing on the degradation and conversion of organic compounds and heavy metals is crucial to provide specific knowledge for responsible authorities in developing pollution control guidelines. While conventional wastewater treatment techniques like adsorption, the Fenton process, and biodegradation have been widely used, they come with limitations such as sludge production, generation of intermediate by-products, and the need for safety measures that’s why research is now inclined towards advanced oxidation products particularly photocatalysis [9].

1.2 Photocatalysis; a viable option

Photocatalysis is an emerging technology that utilizes visible light and photocatalysts for the degradation of pollutants in the environment. Photocatalysts are semiconductors; photon energy can excite the electrons from the Valance Band (VB) of the catalyst to the Conduction Band (CB), generating electron-hole pairs for the redox reaction [10]. Photocatalysis is low-cost, low environmental footprint, and and highly active in pollutant degradation. Photocatalysis harnesses renewable, pollution-free solar energy. Photocatalysis not only reduces the economic burden compared to other treatment methods but also minimizes the generation of secondary waste. Moreover, the photocatalysts employed in the process can be reused, enhancing the cost effectiveness and sustainability of the technology. The implementation of the photocatalysis eliminates the installation of separate, space consuming wastewater treatment plants [11].

1.2.1 Principle of photocatalysis

In photocatalysis, when light energy equal to or greater than the bandgap of the photocatalyst falls on the semiconductor, electrons from the VB move to CB leaving behind holes and initiating the reaction. These electrons and holes can combine within nanoseconds but if given sufficient time they can move to the surface of the catalyst where they can initiate the redox reaction with the pollutant present on the catalyst's surface. Holes in the VB generates hydroxal radical ($OH^{\cdot}$) which facilitates pollutant removal through an oxidation process. Conversely, electrons in the CB reacts with oxygen initiating a reduction process to avoid the accumulation of the excess charges within the catalyst [12].

$$\text{Photocatalyst} + h\nu \rightarrow e^- + h \quad (1.1)$$

$$O_{2(abs)} + e^- \rightarrow O_2^{\cdot -} \quad (1.2)$$

$$H_2O \rightarrow OH^- + H^+ \quad (1.3)$$

$$O_2^{\cdot -} + H^+ \rightarrow HOO^{\cdot} \quad (1.4)$$

$$OOH^{\cdot} + e^- \rightarrow HO_2^- \quad (1.5)$$

$$OOH^- + H^+ \rightarrow H_2O_2 \quad (1.6)$$

The photocatalytic process encompasses distinct steps: firstly, pollutants adsorption on to the catalyst's surface. Following this light absorption occurs, leading to the formation of electron-hole pairs. These charges then migrate to the surface of the catalyst where they may combine. However, if given enough time, instead of recombination charges are harnessed to initiate rection with the pollutant present in the medium.

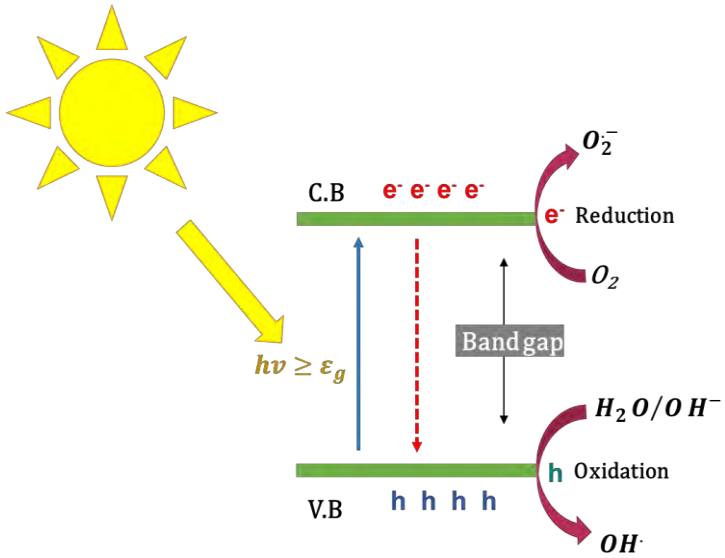

Figure 1.2: Schematics of photocatalytic process.

This reduction and oxidation process results in the formation of radicles that can then react with the pollutant and change them into their respective by-products or form CO_2 and H_2O.

1.2.2 Simultaneous photocatalysis

The utilization of photocatalysis in wastewater treatment has evolved to encompass the simultaneous removal of pollutants. In a simultaneous photocatalytic system, the effective elimination of coexisting pollutants relies on the synergistic interactions between them. Research suggests that in simultaneous pollutant removal, organic compounds undergo oxidation while heavy metals undergo reduction, complementing each other's removal [13]. As demonstrated in the study where FeS_2/Fe_2O_3 was utilized as a catalyst to simultaneously remove carbamazepine and Cr(VI), where the addition of the Cr(VI) enhances the degradation of carbamazepine by scavenging the electron and promoting the electron-hole pair separation [14]. Similarly, $AgI/BiVO_4$ used for tetracycline (TC) and Cr(VI) indicated that TC degradation and Cr(VI) reduction were enhanced in a binary system, suggesting that the coexistence of species that can be oxidized and reduced enhances the utilization of photoinduced carriers [15].

Furthermore, an additional factor impacting the efficiency of simultaneous photocatalysis is ligand-metal charge transfer (LMCT). LMCT typically involves the transfer of an electron from a π^* antibonding ligand orbital to a metal d orbital. Supporting this notion, a study involving the photocatalyst Nb_2O_5 nanorods/graphene demonstrated the simultaneous removal of Cr(VI) and 4-chlorophenol (4-CP). In this scenario, a surface complex of 4-CP and NbO was formed, acting as the electron donor to the conduction band of the catalyst and

operating as LMCT [14]. The dye sensitization effect was observed in the case of the coloured compounds, enhancing the simultaneous photocatalytic removal of the dyes and heavy metals. For example, when $FeVO_4/BiO_4O_5Br/BiOBr$ was employed for the RhB dye removal in a simultaneous system with chromium (VI), it resulted in an increase in Cr(VI) reduction to Cr (III) attributed to the dye sensitization effect [16].

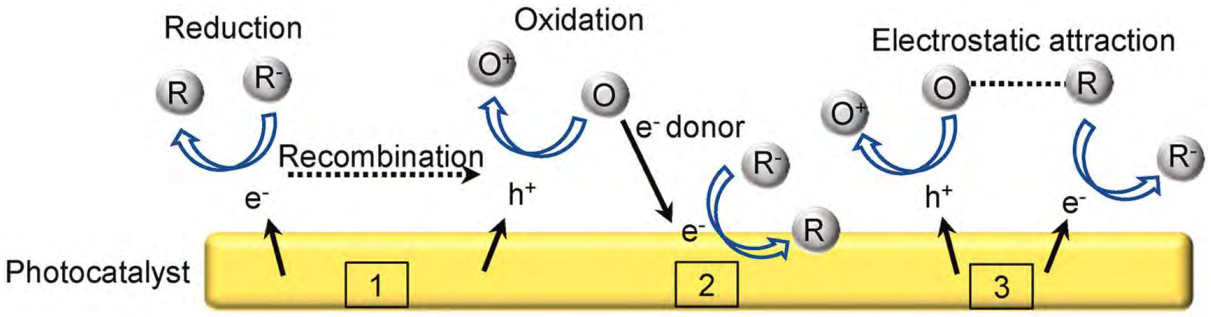

Figure 1.3: Synergism between mixed pollutants in a simultaneous system [3].

Moreover, in a paired pollutant scenario, there's the possibility of one contaminant adsorbing onto the surface of another, creating a complex. This was exemplified in a study involving the concurrent removal of Cr(VI) and berberine hydrochloride (BH) through photocatalysis using P & S co-doped $g\text{-}C_3N_4$. In this instance, the chelating group of BH effectively adsorbed Cr(VI), resulting in an improved removal of Cr(VI) [17]. This highlights how interactions between pollutants play a crucial role in shaping the effectiveness of simultaneous photocatalytic processes. However, the simultaneous removal of the organic compounds with heavy metals does not always complement pollutant removal, as demonstrated in the simultaneous photocatalytic removal of the Cr(VI) and Cu(II) with 4-nitrophenol and phenol over nano anatase-TiO_2. It was found that the reduction of the Cr(VI) and Cu(II) increases in the presence of phenol and 4-nitrophenol while the degradation of phenol and 4-nitrophenol decreases under UV light [16]. Although systems have been developed for the simultaneous removal of organic compounds and heavy metals from wastewater, the interferences of the organic compound in the reduction of the heavy metals have not been fully understood and remain unclear.

Table 1.1: Literature showing simultaneous photocatalytic removal of pollutants.

S. No.	Photoactive catalyst	Pollutants	Light Source	Reaction conditions	Time (h)	Removal (%)	Ref.
1	Au/Pb decorated g-C_3N_4/MCM-41	Phenol Cr (VI)	250 W xenon lamp	**Catalyst** – 50mg **Pollutant concentration** Cr(VI) – 20ppm Phenol - 20ppm **pH** – 5	2 h	Cr(VI) - 91.6% Phenol - 85.4%	[18]
2	$FeVO_4/Bi_4O_5Br_2/BiOBr$	Cr (VI) Rhodamine Blue (RhB)	50 W light LED	**Catalyst** – 100mg **Pollutant concentration** Cr(VI) – 30ppm RhB - 10ppm **pH** – 3	6 h	Cr(VI) – 100% (150min) RhB – 98.2% (360min)	[16]
3	Mesoporous $BiVO_4$	Cr (VI) Methylene Blue (MB)	300 W xenon lamp (UV cut-off Filter)	**Catalyst** – 200mg **Pollutant concentration** Cr(VI) – 10ppm MB – 20ppm **pH** – 1.5	2.5 h	Cr(VI) – 95% MB – 92%	[19]
4	Ag/AgBr/$BiVO_4$	Cr(VI) Ciprofloxacin (CIP)	300 W xenon lamp	**Pollutant concentration** **Cr**(VI) – 10ppm CIP – 10ppm	2 h	Cr(VI) – 100% CIP – 88.21%	[20]
5	Bi_2S_3-$BiVO_4$ graphene aerogel	Cr(VI) Bisphenol A (BPA)	300 W xenon lamp (UV cut-off Filter)	**Catalyst** – 50mg **Pollutant concentration** Cr(VI) – 50ppm BPA – 10ppm **pH** - 2	2 h	Cr(VI) – 100% BPA – 99%	[21]
6	3D flower-like AgI/BiVO4	Cr(VI) Tetracycline (TC)	500 W xenon lamp	**Catalyst** – 0.02g **Pollutant concentration** Cr(VI) – 15ppm TC – 20ppm	1.8 h (100min)	Cr(VI) – 70% TC – 90%	[15]

1.2.3 Limitations of photocatalysis

The application of photocatalysis is limited due to the activity of the photoactive catalyst in UV light, attributed to its band gap $(\varepsilon_g \geq 3.0)$ which only works in UV source. UV light is only 5% of the solar spectrum which limits the process. The other limitation is the mass transfer, the photocatalytic process occurs at the surface of the catalyst when the pollutant comes in contact and is adsorbed on the surface of the catalyst. Often catalyst aggregates within the system limit the light incidence. Additionally, rapid electron-hole recombination poses another challenge [11]. These limitations can be overcome by modification of the photoactive catalyst and optimization of the catalyst synthesis to obtain a catalyst with defined crystal structures and smaller particle sizes [22]. Various modification methods doping (metal and non-metal), surface modification, heterojunction formation, and altering morphology [23,24].

1.3 C_3N_4 nanosheets

Graphitic Carbon Nitride (C_3N_4), the most stable allotrope of the seven Carbon Nitride contains earth-abundant elements such as carbon and nitrogen [23]. C_3N_4 features a band gap of 2.7eV without any metal content. C_3N_4 is easy to prepare, cost-effective, and highly efficient under visible light. C_3N_4 is chemically stable because of the covalent bond present between the carbon and nitrogen of the conjugate layers of triazine and tri-s-triazine motifs as well as thermally stable even at the temperature of 600ºC [25].

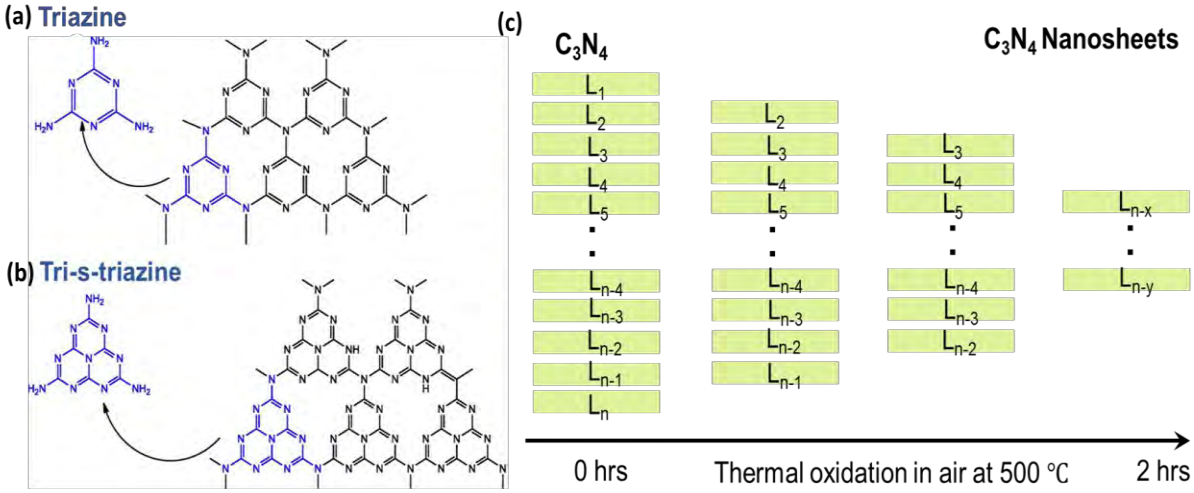

Figure 1.4: (a-b) Triazine and tri-s-triazine motifs present in layered structure of C_3N_4. (c) thermal oxidation process for the formation of C_3N_4 nanosheets [25].

Usually, the photocatalytic activity of the C_3N_4 is low due to the high charge recombination and low specific area [12]. So, to address these limitations C_3N_4 has been subjected to various C_3N_4 nanostructures with optimized physiochemistry and optical properties. However, challenges persist in the form of electron-hole recombination and limited photoactive sites within these nanosheets. This limitation arises from the relatively fewer boundaries and exposed edges in the C_3N_4 nanosheets [26].

1.4 Layered Double Hydroxides (LDHs)

Layered Double Hydroxides (LDHs) or Hydrotalcite compounds are two-dimensional anionic clay material, presented with the formula $[M_{1-x}^{2+}M_x^{3+}(OH)_2(An^{n-})_{x/n}]^{x+}$. mH_2O. Where M^{2+} is divalent ion which may be Mg^{2+}, Cu^{2+}, Ni^{2+}, Co^{2+}, Zn^{2+} while M^{3+} is trivalent ion that can be Al^{3+}, Fe^{3+}, Co^{3+}, Mn^{3+}. While An (CO_3^{2-}, Cl^{-1}, NO_3^{-1}, SO_4^{-2}, PO_4^{-3}) is intercalating anion at the interlayer of LDH [27]. LDHs are made up of brucite-like layers where M^{2+} is coordinated octahedrally by hydroxyl groups. Due to isomorphic substitution divalent cations in LDH can be partially replaced by trivalent cations that form positively charged $M^{2+}M^{3+}$ binary layers of LDH [28].

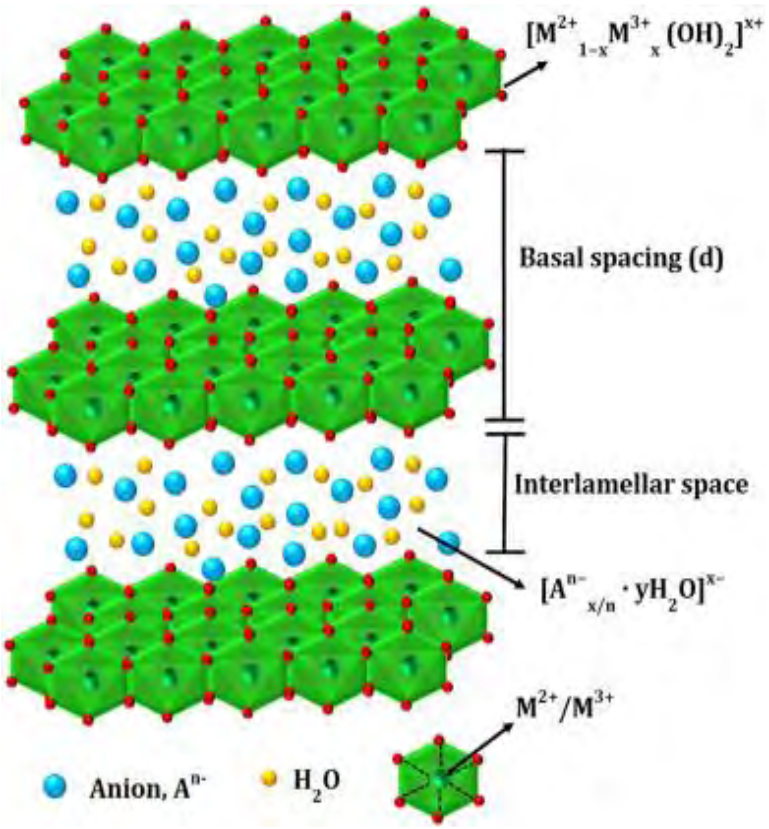

Figure 1.5: The structure of layered double hydroxide with intercalating anion [29].

The metal octahedra in hydrotalcite-like structures are bonded through metal-oxygen-metal oxo linkages. The presence of these linkages is important for the charge transportation from metal to metal which plays a vital role in the charge separation during Photocatalysis. Additionally, the hydroxyl radicle, an essential intermediate in the photocatalytic oxidation event, can be generated via the reaction between the O-H bond perpendicular to the positively charged brucite layer in octahedron and the holes of the valance band. LDH is an excellent catalyst for electrostatic interactions with the intercalating anions owing to the positively charged brucite layers, which favourably increases the specific surface area [29]. LDH-based materials are frequently used for heterogeneous photocatalysis, the Fenton process, and Sulfate radical oxidation because of four exciting features as (1) tunability of metal cation, M^{2+}/M^{3+} Molar ratios, (2) intercalating anionic specie nature, (3) exfoliation of LDH into function ultrathin layers and (4) reconstruction of LDH through ‘’memory effect’’ [30].

1.4.1 CuNiFe LDH

CuNiFe LDH is a highly efficient and active catalyst in the application of the Fenton process, Persulfate photocatalytic degradation, and HC-SCR technology. CuNiFe LDH has a suitable bandgap for working in visible light. CuNiFe LDH can reduce the e^--h recombination, is stable, and high surface area that makes it suitable for photocatalytic application [31].

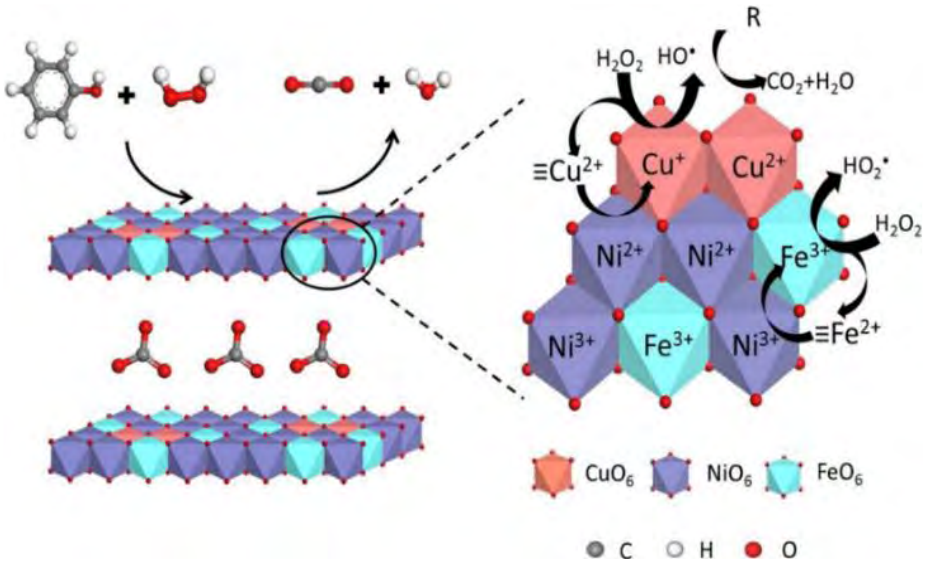

Figure 1.6: Possible structure and degradation pathway of organic compounds over CuNiFe LDH [31].

1.5 Proposed system

C_3N_4 is extensively studied photoactive catalyst for the removal of pollutants from wastewater, yet it faces the issue of high charge recombination rate. On the other hand, CuNiFe LDH potential as photoactive catalyst remains largely unexplored. To tackle this, we synthesized C_3N_4 nanosheets with increased surface area via thermal condensation and thermal oxidation. However, electron-hole recombination posed a challenge. To address this, we developed a composite CuNiFe LDH/C_3N_4 nanosheets to effectively minimize the recombination rate.

1.6 Problem statement

Removal of pollutants from environmental matrices is a complex phenomenon. For practical realisation of photocatalytic systems for environmental remediation, better control and a deeper understanding of active systems is a pressing challenge. Apart from that how the concurrent occurrence of different pollutants influences their removal is rather overlooked. So, there is need to investigate more of photooxidation of pollutants (organics) and photoreduction of heavy metals (Cr).

1.7 Aims and objectives

1. Synthesize CuNiFe LDH/C_3N_4 nanosheets composite.
2. Investigate the photocatalytic activity of synthesized catalysts on Cr(VI) and 4-NP.
3. Examine the simultaneous photocatalytic activity of the synthesized catalyst for both Cr(VI) and 4-nitrophenol (4-NP), 2-chlorophenol (2-CP), and levofloxacin (LEV).
4. Explore the effect of different conditions on the photocatalytic reduction of Cr(VI).
5. Evaluate reusability and mechanism involved in the degradation of targeted pollutants.

2. MATERIALS AND METHODS

This chapter presents a comprehensive insight into the materials used and procedures employed for catalysts synthesis. It also encompasses details of procedures and instrumentation utilized for characterizing and conducting photocatalytic tests on the synthesized catalysts. This chapter will offer a clear understanding of the approaches and techniques employed to achieve the research objective outlined in the previous chapter.

The following catalysts are synthesized.

1. CuNiFe LDH
2. Carbon Nitride (C_3N_4) nanosheets
3. 1:1 (CuNiFe LDH/carbon nitride nanosheets)
4. 1:2 (CuNiFe LDH/carbon nitride nanosheets)
5. 1:3 (CuNiFe LDH/carbon nitride nanosheets)
6. 2:1 (CuNiFe LDH/carbon nitride nanosheets)
7. 3:1 (CuNiFe LDH/carbon nitride nanosheets)

The same precursor materials are used in the synthesis of all samples and the same method is applied to ensure efficient synthesis.

2.1 Materials for synthesis

Analytical grade materials are employed without any additional purification for synthesis. $C3N4$ nanosheets are synthesized by using melamine. For the preparation of CuNiFe LDH, Copper (II) nitrate trihydrate ($Cu(NO_3)_2.3H_2O$), Nickel (II) nitrate hexahydrate ($Ni(NO_3)_2.6H_2O$), Iron (III) nitrate nonahydrate ($Fe(NO_3)_3.9H_2O$) is used. For pH adjustment sodium hydroxide (NaOH) and sodium carbonate (Na_2CO_3) is used. All the chemicals were purchased from DAEJUNG Chemicals and Metals. For photocatalytic testing Potassium Dichromate ($K_2Cr_2O_7$) and 4-Nitrophenol (4-NP) were used.

2.2 Methods for synthesis

Thermal polymerization of melamine was conducted in a muffle furnace for the preparation of C_3N_4 in bulk. For C_3N_4 nanosheets, this material was subjected to thermal exfoliation.

Coprecipitation is a common technique for LDH synthesis. In this method, divalent and trivalent cations containing anions are dissolved in an aqueous solution. The cations create the layered structure while anions intercalate. An alkali solution will be utilized for

coprecipitation of the cations. Thermal aging enhances the product purity and crystallinity. This process also requires prolonged washing for the reduction of residual alkali. The mechanism relies on hexa-aqua metal complex formation in a solution, yielding brucite-like layers with evenly distributed metallic cations and intercalated anions [32].

Sonication is a vital process in materials preparation, involving agitation of particles in a liquid with the application of sound energy. The frequency of ultrasonication is between 20-40 kHz. The frequency, power, and duration of ultrasonication plays a critical role in determining the material stability [33].

2.3 Synthesis of C_3N_4 nanosheets

C_3N_4 nanosheets were prepared through thermal condensation followed by thermal exfoliation using melamine as a precursor [26]. In detail, melamine was heated at 550 ℃ for 4 h at a ramp rate of 2 ℃/min. The resultant yellow powder was ground in a pestle and mortar. Following the grinding step, the prepared bulk C_3N_4 was subjected to thermal exfoliation where Bulk C_3N_4 was re-heated in an open container at 500 ℃ for 4 h at a ramp rate of 5 ℃/min.

Figure 2.1: Schematics of synthesis of C_3N_4 nanosheets

2.4 Synthesis of CuNiFe LDH

Co-precipitation method was used for the preparation of CuNiFe LDH [31]. In detail, the mixed metal salt solution in 200 mL deionized water was prepared by adding 0.025 mol of $Cu(NO_3)_3.3H_2O$, 0.025 mol of $Fe(NO_3)_3.9H_2O$ and 0.0625 mol of $Ni(NO_3)_2.6H_2O$. An alkaline solution containing 0.8 M NaOH and 0.2 M Na_2CO_3 was prepared afterward. The pH of the mixed metal salt solution was adjusted to 10 by adding the alkaline solution dropwise. This resulting suspension was stirred for 30 min, follow by aging at 80 ℃ for 24 h. Later, the resultant was centrifuged, washed repeatedwith deionized water several times, and then oven dried for 12 h at 80 ℃.

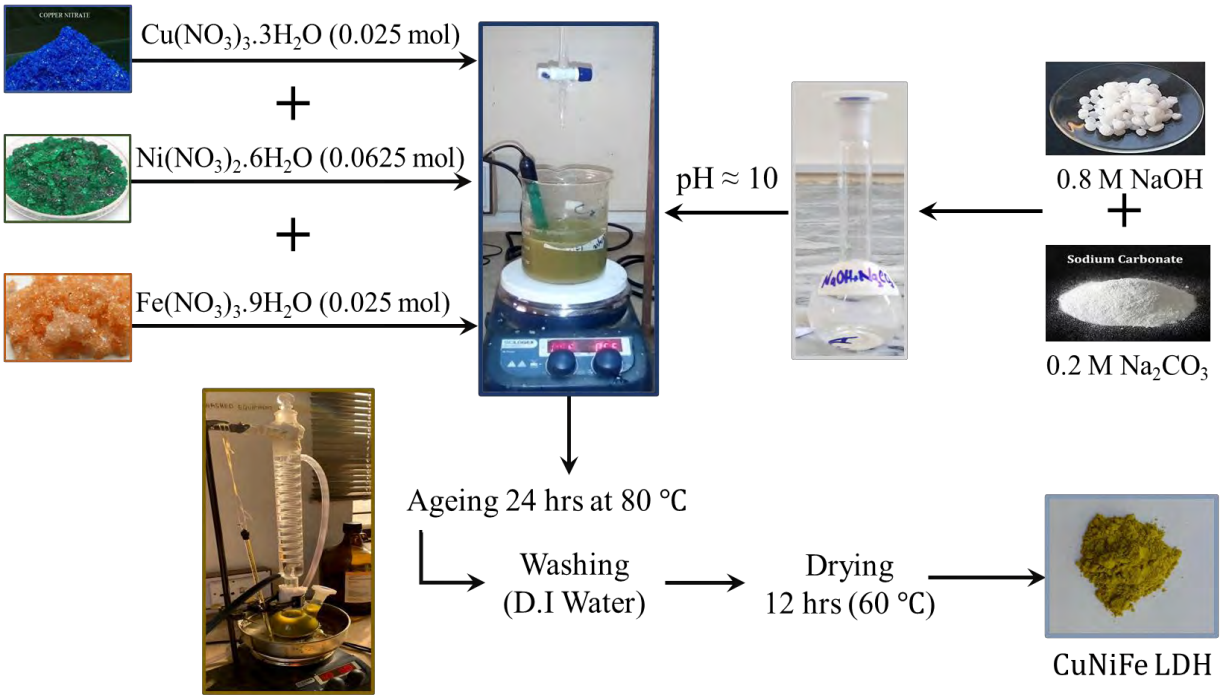

Figure 2.2: CuNiFe LDH synthesis through the coprecipitation method

2.5 Composite synthesis

CuNiFe LDH/C_3N_4 composite of different ratios (1:1, 1:2, 1:3, 2:1, 3:1) were prepared. Simply, a certain amount of C_3N_4 nanosheets was dispersed in 20ml of ethanol through sonication for 30 min. After that a certain amount of CuNiFe LDH was added into the dispersed solution and sonicated for 2 hrs. The resultant mixture was then dried at 60 ˚C until the evaporation of ethanol.

2.6 Characterization

In the area of nanomaterials research, the ability to understand and analyze the structural, optical, and chemical properties of materials is of primary significance. Here, the characterization techniques used to investigate structural and optical attributes of materials are briefly explained. We employed UV-Vis spectrophotometry, PL, SEM, XRD, and FTIR to comprehensively examine the properties of CuNiFe LDH and C_3N_4 nanosheets.

2.6.1 X-ray Diffraction (XRD)

X-ray diffraction is an analytical tool used for the phase identification, crystallinity, impurities in materials as well as information about the unit cell. The fundamental principle of XRD involves the constructive interference between monochromatic x-rays and crystalline samples. This interference will be produced when the conditions satisfy Bragg's law:

$$n\lambda = 2\,d\sin\theta \qquad 2.1$$

where, n is any integer displaying the order of diffraction, λ is wavelength of the incident x-ray beam, d is the spacing between crystal lattice planes while θ is Bragg's angle of diffraction from different planes [34].

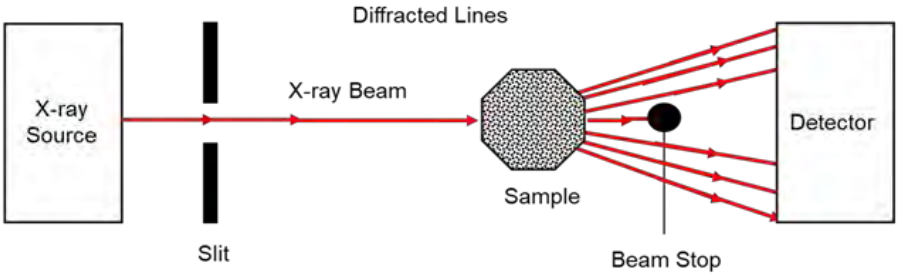

Figure 2.3: Working of X-ray diffraction [34].

X-rays are generated in the cathode ray by producing electrons from a heated filament. These electrons can be accelerated and bombarded on the targeted material, causing the dislocation of inner shell electrons, and generating x-rays. Monochromatic x-rays are then directed onto the sample, and the intensity of reflected x-rays will be recorded. When the incident x-rays align with Bragg's equation, constructive interferences lead to peak formation [35,36].

2.6.2 Scanning Electron Microscopy (SEM)

Scanning electron microscopy (SEM) is a powerful technique in characterization for surface imaging, topography, and composition of the material. It employs a focused electron beam on the sample's surface, generating signals through electron-atom interactions that reveal composition and morphology [37]. An electron gun will produce a beam of electrons that travels down the vacuum path within the microscope. Electromagnetic field and lenses focus this beam onto the sample's surface. When the electron beam hits the sample, it

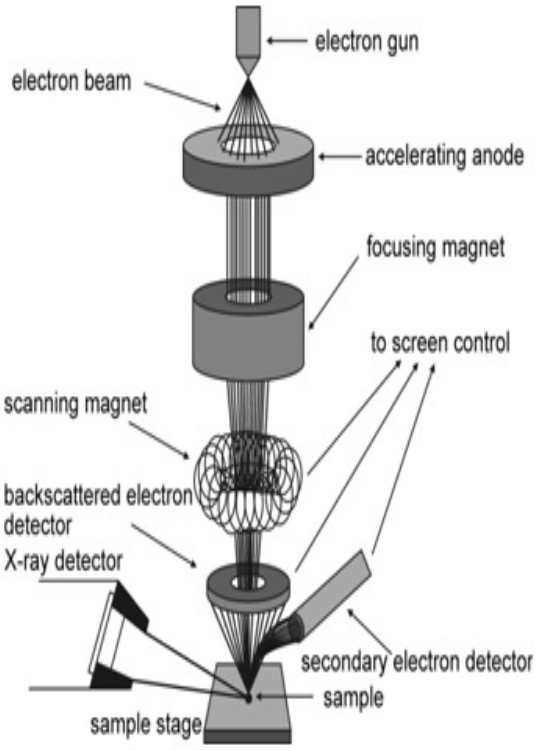

Figure 2.4: Schematic diagram of SEM [38].

causes the release of the electrons and x-rays. A detector gathers these particles and converts them into a signal, which is then displayed as an image on a monitor [38].

2.6.3 UV-Vis Diffuse Reflectance Spectroscopy (UV-DRS)

UV-Vis DRS is a technique used for analysing powders and surfaces by measuring the diffuse reflectance of UV-Vis radiations. The UV-Vis beamis directed at an angle onto the sample and, resulting in radiation reflection [39]. The reflected radiation can be regular or diffuse. When radiation hits a smooth and planar surface, reflected at an angle equal to the angle of incidence it will be regular reflectance. On the other hand, diffuse reflectance is a combination of some optical phenomena such as reflection, scattering, diffraction, absorption, and refraction in all directions [40].

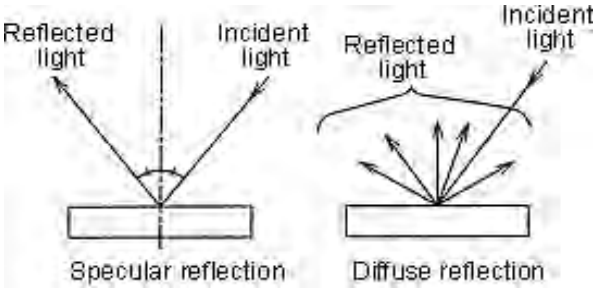

Figure 2.5: Diffuse Reflectance spectra conceptualization [41].

The most widely used model is the Kubelka-Munk function. All the geometric abnormalities of the inhomogeneous samples were reduced into a single parameter, the scattering coefficients. The scattering coefficients account for the internal scattering processes, dominated by the particle size and refractive index.

$$\frac{k}{s} = \frac{(1-R_\infty)^2}{2R_\infty} = FR_\infty \qquad 2.2$$

Where, FR_∞ is the Kubelka-Munk (K-M) function, R_∞ is reflectivity, k is Kubelka-Munk absorption coefficient while s is Kubelka-Munk scattering coefficient.

2.6.4 Photoluminescence spectroscopy

Photoluminescence is caused by photon absorption which leads to photoexcitation and then the emission of the photon when electrons deexcite. Here we use PL for the investigation of the separation of the charge carriers as the PL signal is the result of the recombination of the photogenerated electron-hole pairs. It is a contactless and non-destructive phenomenon [42].

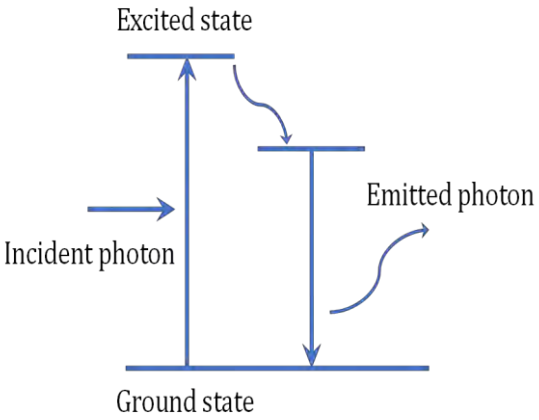

Figure 2.6: Conceptualization of photoluminescence [42].

2.6.5 Instruments and methods employed for characterization

X-ray diffraction (XRD) profiles were obtained by employing a PANalytical X'Pret Pro diffractometer equipped with a Cu Kα radiation source (λ=1.5418Å), generated at 40kV and 40 mA. Photoluminescence (PL) measurements were conducted with a time-correlated single photon counting (TCSPC) setup (FluoTime300, PicoQuant GmbH), where a 405nm laser was pulsed at a frequency of 32M. The optical properties of the as-synthesized samples were analyzed using the diffuse reflectance spectroscopy technique (DRS) with a UV-VIS spectrometer (PerkinElmer, Lambda 950, maximum power 250 VA) that included an integrated sphere. SEM images were captured using a JEOL 6500F FEG SEM operating at 5KV with a working distance of 10mm. For FTIR analysis, Thermo Scientific Nicolet 6700 Fourier transform infrared spectrometer (FTIR), in the range of 500-4000cm^{-1}.

2.7 Photocatalytic activity testing

To investigate the photocatalytic activity of the CuNiFe LDH/C_3N_4, the synthesized catalysts (0.1g/L) were dispersed in the aqueous solution of $K_2Cr_2O_7$ (10ppm). Prior to sunlight irradiation of the solution, the suspension was kept in darkness for 30min to achieve adsorption-desorption equilibrium. After that, this suspension was transferred to sunlight and samples were collected every 30 min. The catalyst was separated from suspension through centrifugation (5000rpm, 4min). UV-Vis spectrum for Cr(VI) was obtained through the diphenyl carbazide (DPC) method at 540nm [43]. An experiment without the addition of a catalyst was also carried out. The photocatalytic degradation efficiency was calculated by using the formula [44]:

$$\% \text{ Degradation} = \frac{C_0 - C_t}{C_0} \times 100 \qquad 2.3$$

Where C_0 and C_t represent the initial concentration and concentration at different times of the targeted pollutants respectively. The reaction kinetic was determined using the pseudo-first-order reaction kinetic model as follows [44];

$$\ln \frac{C_0}{C_t} = k_{app} t \qquad 2.4$$

Where k_{app} represents the apparent pseudo-first-order rate constant (min^{-1}).

The photodegradation of organic compound (4-NP, 2-CP, and LEV) was also investigated using the CuNiFe LDH/C_3N_4. For this purpose, the synthesized catalyst (0.1g/L) was dispersed in an aqueous solution of 4-NP (10ppm). The solution was stirred in dark to attain adsorption-desorption equilibrium. The suspension was then irradiated in sunlight and samples were collected every 30min. After centrifugation (5000rpm; 4min), a UV-Vis spectrum of 4-NP was obtained through a UV-Vis spectrophotometer.

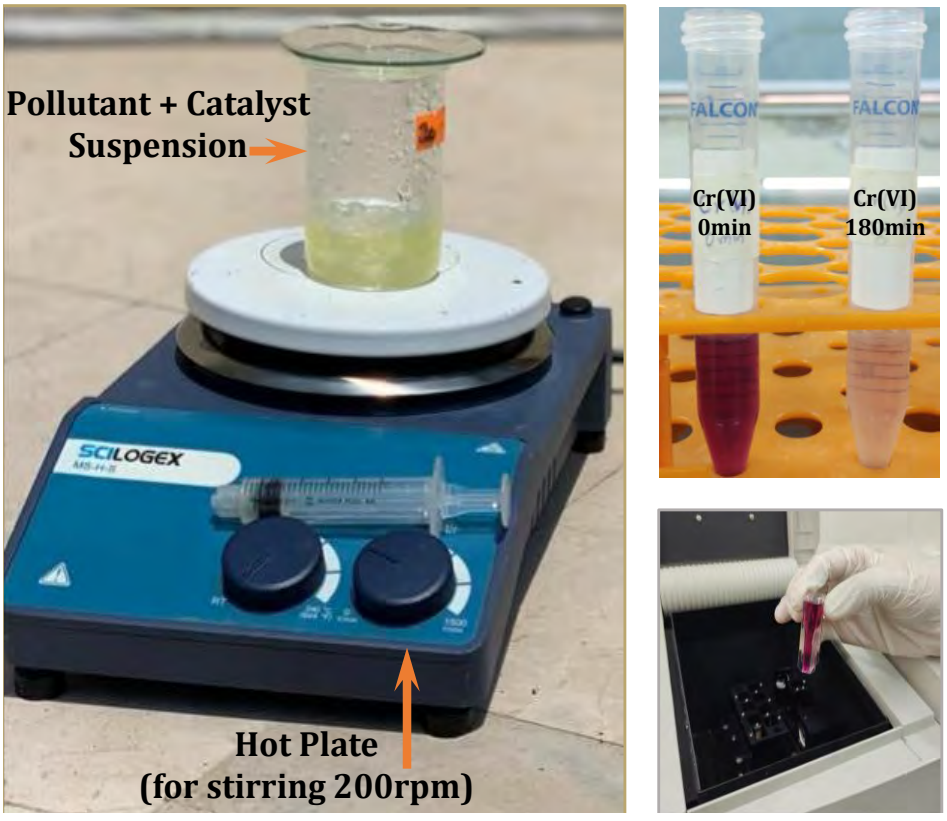

Figure 2.7: Experimental Setup for photocatalytic activity testing

3. RESULTS AND DISCUSSION

This chapter presents the compiled results obtained from a range of characterizations and photocatalytic activity experiments. The prime focus of the study is the understanding of the structural, chemical, and optical properties of the synthesized catalysts C_3N_4 nanosheets, CuNiFe LDH, and their ratios. The techniques used for this purpose are PL, UV-DRS, FTIR, SEM, and XRD. In addition, this chapter provides a comprehensive presentation of the outcomes resulting from the photocatalytic activity tests for Cr(VI) and 4-NP. Through a series of carefully designed experiments, we aim to understand the material's efficiency in removing these pollutants under natural conditions.

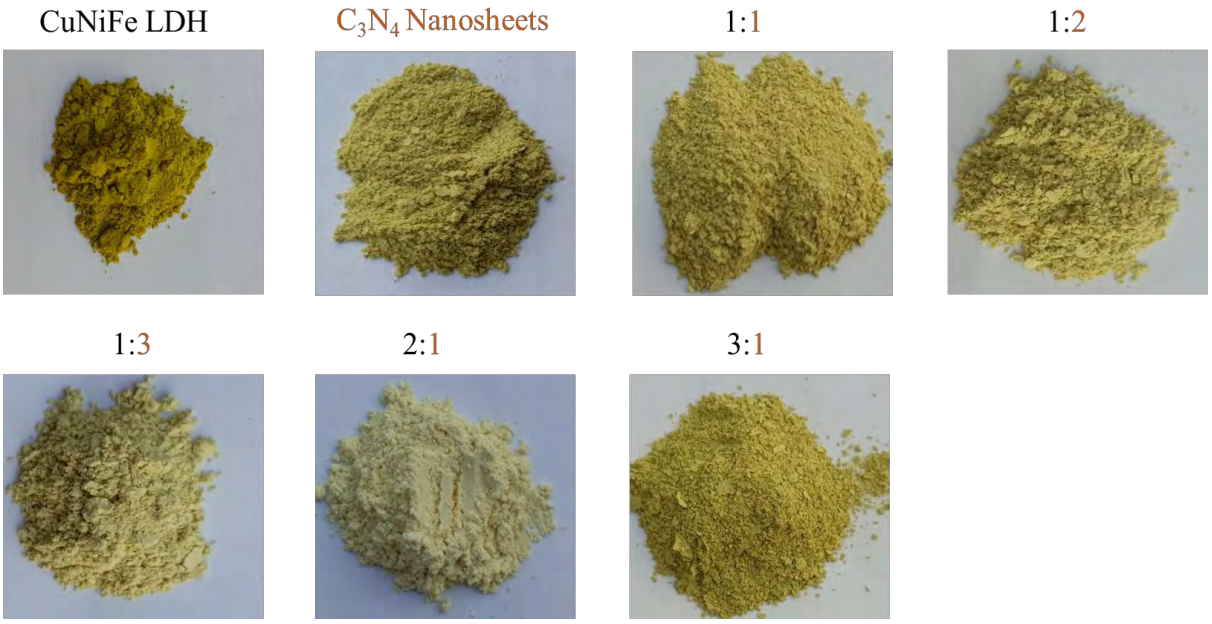

Figure 3.1: Prepared catalysts CuNiFe LDH, C_3N_4 nanosheets, 1:1, 1:2, 1:3, 2:1, and 3:1.

3.1 Scanning Electron Microscopy

The SEM images of the CuNiFe LDH, C_3N_4 nanosheets and the composite 1:2 (CuNiFe LDH/C_3N_4) is shown in **Figure 3.2**. CuNiFe LDH shows a layered structure with dispersed octahedral structure. While C_3N_4 displayed a relatively smooth surface with a lamellar structure lacking clearly defined boundaries. While the composite of the CuNiFe LDH/C_3N_4 shows the presence of the loose lamellar structure over layered structure that that are the characteristic features of pristine catalyst. EDX analysis shows that CuNiFe LDH contains characteristic O, Cu, Ni, and Fe while composite along with the O, C, and N of C_3N_4 also contains Ni and Fe of CuNiFe LDH.

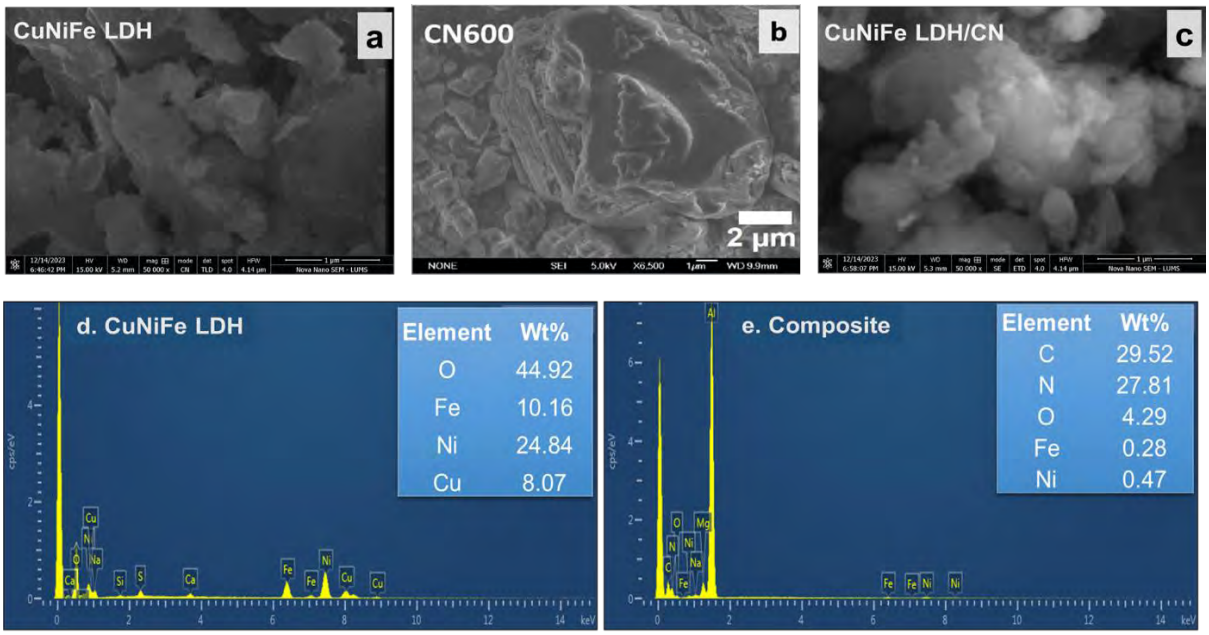

Figure 3.2: SEM analysis of a) CuNiFe LDH b) C_3N_4, and c) CuNiFe LDH/C_3N_4 (1:2) and EDX analysis of d) CuNiFe LDH and e) composite 1:2.

3.2 X-ray Diffraction

XRD patterns of pristine CuNiFe LDH, C_3N_4 nanosheets, and their composite 1:1 and 1:2 is presented in **Figure 3.3.** As shown in the figure C_3N_4 nanosheets exhibit two diffraction peaks at 27.45 ̊and 13.0 ̊ corresponding to the (002) and (100) crystal plane respectively. The peak at 27.45 ̊may be attributed to the interlayer stacking while peak at 13.0 ̊ corresponds to the heptazine units [45].

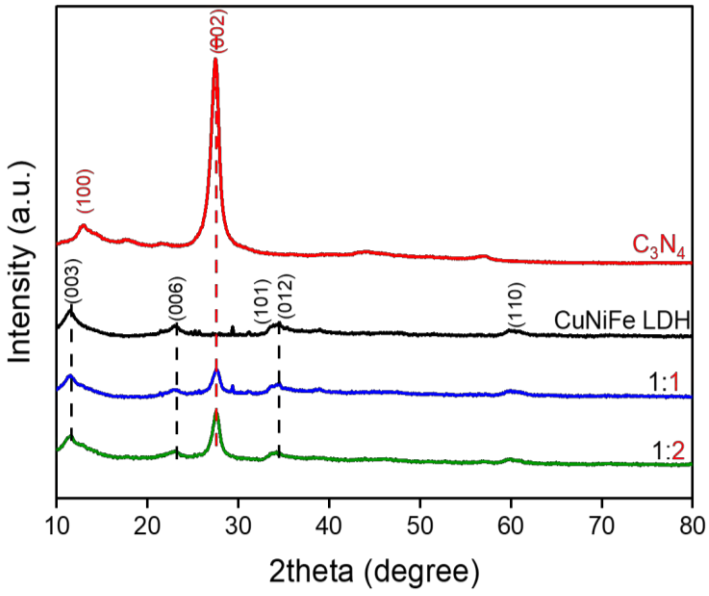

Figure 3.3: XRD pattern of CuNiFe LDH, C_3N_4 nanosheet and their composites (CuNiFe LDH/C_3N_4 nanosheet).

In CuNiFe LDH, a series of reflection around 11.37°, 22.8°, 34.57° and 59.82° can be assigned to (003), (006), (012) and (110) crystal planes respectively. These diffraction peaks are the characteristic of hydrotalcite like structure of LDH [46]. All the diffraction peaks of the CuNiFe LDH could be displayed in the composites 1:1 and 1:2 while only one characteristic plane (002) of C_3N_4 nanosheets could be displayed in the composites.

3.3 Electronic properties of photocatalyst

Electronic properties of photocatalysts were determined through photoluminescence ad UV-DRS. Photoluminescence spectra was recorded to check the recombination process of the photogenerated electron-holes carriers of the catalysts. Higher intensity of the photoluminescence encodes for higher recombination rate of electron-holes. The photoluminescence radiation spectra's for CuNiFe LDH, C_3N_4 nanosheets and their ratios were obtained using pure ethanol solvent. **Figure 3.4 (a)** presents the PL spectra of the prepared materials. A broad intensity peak for C_3N_4 nanosheets at around 450nm was recorded while an emission peak for CuNiFe LDH at around 405nm shows the luminous recombination of the electron-holes pair. As observed, the peaks show a clear decrease in the recombination rate for the ratios as compared to the pristine C_3N_4 nanosheets. The C_3N_4 nanosheets has highest recombination rate, as the composite formed the recombination rate decreases. 1:2 (CuNiFe LDH/C_3N_4 nanosheets) shows the lowest recombination rate.

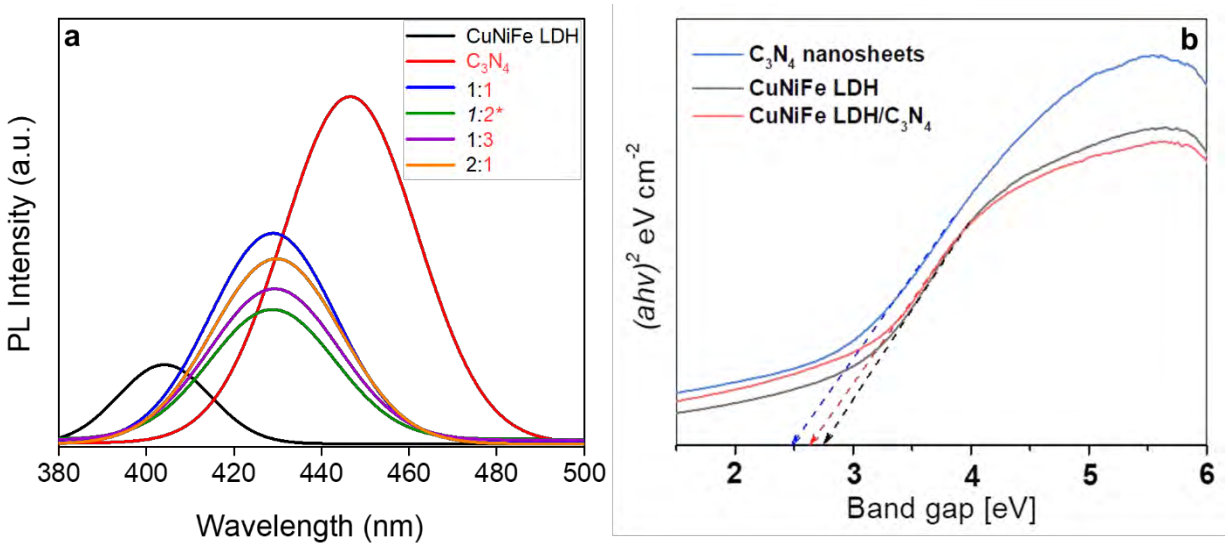

Figure 3.4: (a) Photoluminescence Spectra and **(b)** UV-DRS of the as prepared samples of CuNiFe LDH, C_3N_4 Nanosheets and their composite (CuNiFe LDH/C_3N_4 Nanosheets).

UV-DRS analysis was conducted to determine the band gap of photocatalyst. Kulbeka-Munk function was applied for the determination of band gap. C_3N_4 nanosheets shows a band gap of 2.5eV while CuNiFe LDH showed band gap of 2.8eV (**Figure 3.4 (b)**). When composite was formed band gap shifted to 2.7eV which means that electronic structure has been modified.

3.4 FTIR spectra

FTIR spectra of the CuNiFe LDH, C_3N_4 Nanosheets and their composite (CuNiFe LDH/C_3N_4 nanosheets) of different ratios is presented in the **Figure 3.5** For CuNiFe LDH, two broad bands around 3300 cm^{-1} and 1647 cm^{-1} are ascribed to the stretching vibration of hydroxyl and bending vibration of water. A sharp peak at 1347 cm^{-1} in CuNiFe LDH is attributed to the asymmetric stretching vibration of carbonate ions which means that the carbonate is the primary compensation anion in the interlayer of CuNiFe LDH [47,48]. A strong adsorption band between 3000-3300 cm^{-1} in C_3N_4 nanosheets is assigned to N-H vibrations.

3:1

Figure 3.5: FTIR spectra of CuNiFe LDH, C_3N_4 nanosheets and their composite, FTIR spectra from 640-520 cm^{-1} is presented separately.

For the composites of CuNiFe LDH/C_3N_4 nanosheets broad band between 3000-3700 cm^{-1} is assigned to the stretching vibrations of O-H and N-H bonds. In C_3N_4 nanosheets and all the composites, several vibration bands between 1200-1700 cm^{-1} can be related to aromatic C-N heterocycle while a sharp band near 804 cm^{-1} can be originated from bending vibration of tri-s-triazine units [49,50]. A series of band below 600 could be attributed to the vibrations of M-O

and O-M-O in octahedral sites [47]. Results indicates that the structure of the C_3N_4 nanosheet is maintained even after the formation of composite. There are no peaks in the composite except for the one present in CuNiFe LDH and C_3N_4 nanosheets that suggests that there is no impurity component formation during synthesis.

3.5 Photocatalytic activity

The photocatalytic activity of the synthesized catalysts was evaluated through inorganic pollutant, Cr (VI) and organic pollutants such as 4-nitrophenol (4-NP), 2-chlorophenol (2-CP), and levofloxacin (LEV). All the prepared catalysts were tested for their photocatalytic activity in direct sunlight with lux between 110,000-130,000. 100ppm stock solution of $K_2Cr_2O_7$ for Cr (VI) reduction and pure 4-NP, 2-CP, and LEV for their degradation was prepared. Further, from this stock solution 10ppm of 50ml solution was prepared for respective pollutant. 0.1g/L of each catalyst was added to each photocatalytic experiment. Solutions were placed in the dark for 30 min for adsorption and then shifted to open air under sunlight for photocatalytic activity for 3 hrs. It is important to keep the solution with photocatalyst in the dark to attain adsorption-desorption equilibrium as for photocatalysis the contact of the pollutant with the surface of the photocatalyst is important. The decrease in the concentration of the pollutant is because of the phenomenon of both, adsorption and photocatalysis. Samples were taken after every 30 minutes, and absorbance was recorded through UV-Vis spectrophotometer.

3.5.1 Evaluation of photocatalytic activity

Cr(VI), 4-NP, 2-CP, and LEV removal using the synthesized photocatalysts under solar irradiation was measured through UV-Vis spectrophotometer. The UV-VIS absorbance for Cr(VI) was measured through DPC method. For this purpose, the pH of the samples was adjusted to 2 ± 0.5 and 0.1mL of 1,5 diphenyl carbazide solution was added to every 5mL of sample. Absorbance was measured after 5 min when the colour was fully developed. Peak for Cr(VI)-DPC complex was recorded at 540nm. **Figure 3.6 (a)** shows a clear decrease in absorbance from 0 min to 180 min which indicates the reduction of Cr (VI) to Cr (III). For 4-NP the absorbance peak was found at 317 nm, for 2-CP at 274 nm while for LEV at 306 nm as shown in **Figure 3.6 (b-d)** that also shows a clear decrease in the peak from 0 min to 180 min which is attributed to the degradation of the pollutants.

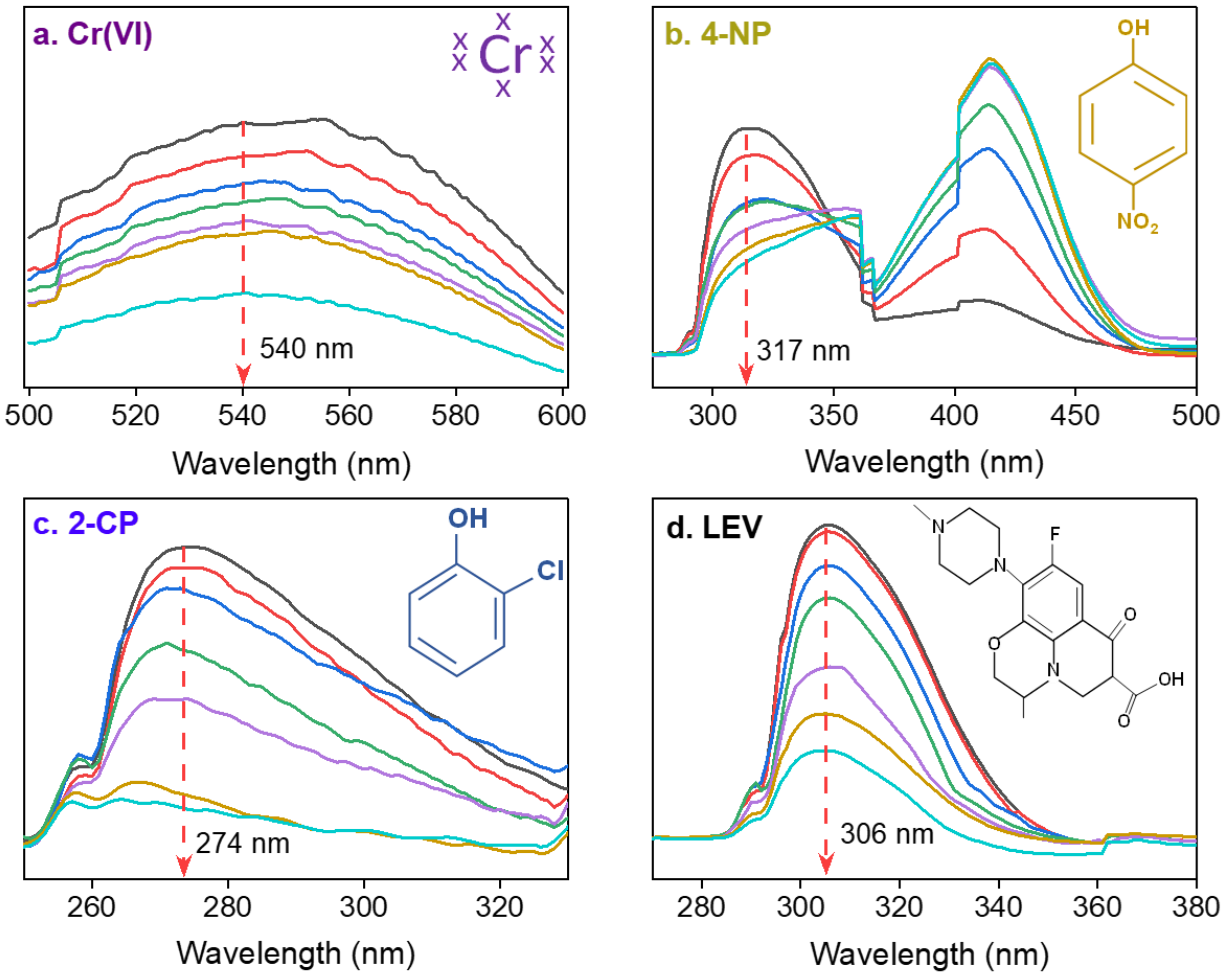

Figure 3.6: Activity profiles of (a) Cr(VI), (b) 4-NP, (c) 2-CP, and (d) LEV.

3.5.2 Photocatalytic testing of targeted pollutants

The photocatalytic removal of the Cr(VI) and 4-NP was examined without catalysts (photolysis), and with pristine catalysts such as CuNiFe LDH and C_3N_4 nanosheets. Without catalyst, both Cr(VI) and 4-NP shows negligible removal and with CuNiFe LDH and C_3N_4 nanosheets, Cr(VI) shows a removal of 23.7% and 21.7% while 4-NP shows a removal of 26.8% and 17.3%, respectively (**Figure 3.7 and 3.8).** After that composites of CuNiFe LDH and C_3N_4 nanosheets were formed in different ratios. Out of these ratios 1:2 showed the highest percent removal for both pollutants i.e., Cr(VI) and 4-NP. The trend shows that as we increased the C_3N_4 ratio from 1 to 2, keeping CuNiFe LDH ratio constant the removal rate increased while further increase didn't result in any further increase of the pollutant removal. On the other hand, increase in CuNiFe LDH concentration.

Further, kinetics of the reaction was determined using the formula.

$$C(t) = C_0 e^{(-kt)} \qquad 3.1$$

Where, kt is molar distinction coefficient. The rate of reduction k/min is the value of slope obtained from -ln (C_t/C_0) vs time plot.

Figure 3.7: Photocatalytic reduction of Cr(VI) over pristine catalyst and ratios, highlighting that 1:2 showed superior catalytic activity compared to others.

Figure 3.8: Photocatalytic degradation of 4-NP over pristine catalyst and ratios, highlighting that 1:2 showed superior catalytic activity compared to others.

After photocatalytic testing of the Cr(VI) and 4-NP over all the prepared catalyst and from the results of photoluminescence we got 1:2 as the best working ratio. All the remaining photocatalytic experiments were conducted utilizing 1:2 as photocatalyst. **Figure 3.9** shows the percentage reduction of Cr (VI), 4-NP, 2-CP, and LEV over CuNiFe LDH/C_3N_4 (1:2)

under sunlight. Cr(VI) shows a removal percentage of 62.3% while 4-NP, 2-CP and LEV shows a removal percentage of 59.15%, 57.5%, and 63.59%, respectively. this means that the prepared catalyst has ability to remove the targeted pollutants.

Figure 3.9: Percentage removal of targeted pollutants over 1:2 (pollutant concentration – 10ppm, photocatalyst – 5mg).

3.5.3 Simultaneous removal of organic compounds and Cr(VI)

The photocatalytic activity performance for Cr (VI), 4-NP, 2-CP, and levofloxacin was examined in a single system over 1:2 (CuNiFe LDH/C_3N_4), which was found to be the best working ratio among the pristine and other ratios. The photocatalytic reduction of Cr (VI) to Cr (III) was found to be 61.23% while for 4-NP, 2-CP, and levofloxacin, the removal percentage was 59.15%, 57.5%, and 63.59%, respectively (**Figure 3.10**). When the photocatalytic reduction of Cr (VI) was carried out simultaneously in the presence of organic compounds, Cr (VI) reduction was changed for each organic compound. In the presence of 4-NP the Cr (VI) reduction increases to 72% from 61.23% while the 4-NP removal decreases to 19.86% with the pH 4 of the suspension. This change in the removal of pollutants can be attributed to the oxidizing nature of the -NO_2 group attached to the phenolic ring in 4-NP, which leads to the competition of electron withdrawal between Cr (VI) and 4-NP. In the case of photocatalytic reduction of Cr (VI) in the presence of 2-CP at pH 5, Cr (VI) reduction decreases to 40.94% while 2-CP removal increases to 88.37%. The underlying reason for this change may be because of the chemical nature of 2-CP which can withdraw an electron which is its inductive effect as well as donate an electron because of the resonance effect of the ring. The Cr (VI) reduction in the presence of levofloxacin results in an increase in the

photocatalytic reduction of Cr (VI) to 77.56% and removal of levofloxacin to 68.66% at pH 4. This increase in the removal percentages may be attributed to the utilization of the electrons by Cr (VI) while the scavenging of holes by levofloxacin leads to the enhanced reduction of Cr (VI) and oxidation of levofloxacin.

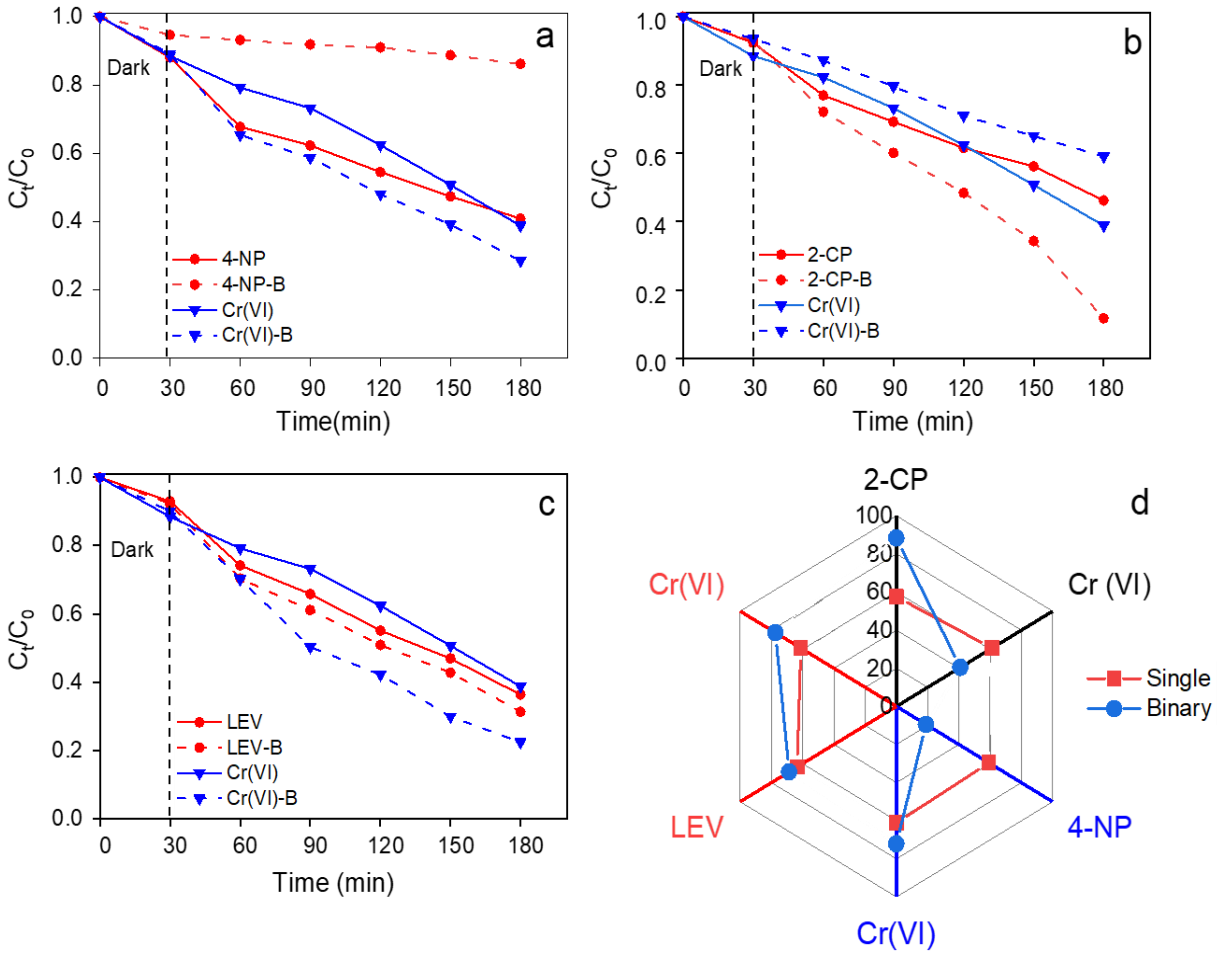

Figure 3.10: Simultaneous photocatalytic activity: C_t/C_0 results (a) Cr-4NP, (b) Cr(VI)-2CP, (c) Cr(VI)-LEV, and (d) removal percentages of all the reaction.

The linear fitting curve of $\ln(C_t/C_0)$ against time suggests that pollutant removal follows a pseudo-first-order reaction. **Table 3.1** presents the overall reaction kinetics of pollutant removal in both single and binary systems using a 1:2 photocatalyst. The data reveals an increase in the removal rate of Cr(VI) from $4.99*10^{-3} \pm 4.62*10^{-4}$ to $6.8*10^{-3} \pm 3.67*10^{-4}$ and $8.56*10^{-3} \pm 4.36*10^{-4}$ with the addition of 4-NP and LEV, respectively. However, in the presence of 2-CP, the removal rate decreases to $2.99*10^{-3} \pm 1.05*10^{-4}$, which is almost three times less than the Cr(VI) reduction in the presence of LEV. Interestingly, the removal rate of 4-NP decreases significantly in the presence of Cr(VI) from $4.93*10^{-3} \pm 2.51*10^{-4}$ to

$7.15*10^{-4} \pm 7.99*10^{-5}$. Conversely, for 2-CP and LEV, the removal rates increase by 2.5 and 0.5 folds, respectively.

Table 3.1: Rate constant and percentage of targeted pollutants in single and simultaneous system

System	Pollutant	Removal Rate K^{-1}	Percentage
Cr(VI)+4-NP	4-NP	$4.93*10^{-3} \pm 2.51*10^{-4}$	59.15
	4-NP-B	$7.15*10^{-4} \pm 7.99*10^{-5}$	19.856
	Cr(VI)	$4.99*10^{-3} \pm 4.62*10^{-4}$	61.23
	Cr(VI)-B	$6.8*10^{-3} \pm 3.67*10^{-4}$	71.45
Cr(VI)+2-CP	2-CP	$4.21*10^{-3} \pm 1.85*10^{-4}$	57.5
	2-CP-B	$1.05*10^{-2} \pm 2.01*10^{-3}$	88.37
	Cr(VI)	$5.04*10^{-3} \pm 4.79*10^{-4}$	61.23
	Cr(VI)-B	$2.99*10^{-3} \pm 1.05*10^{-4}$	40.94
Cr(VI)+LEV	LEV	$5.62*10^{-3} \pm 2.66*10^{-4}$	63.59
	LEV-B	$6.36*10^{-3} \pm 3.54*10^{-4}$	68.66
	Cr(VI)	$4.99*10^{-3} \pm 4.62*10^{-4}$	61.23
	Cr(VI)-B	$8.56*10^{-3} \pm 4.36*10^{-4}$	77.56

Table 3.2: Comparison of simultaneous removal of Cr(VI) and organic compounds with literature

System	Pollutants	Parameter	Removal Efficiency	Ref.
Natural melamine/TiO_2	Cr(VI) – Methyl orange	MO – 10 mgL^{-1} Cr(VI) – 30 mgL^{-1}	Cr(VI) – 99.99% MO – 99.99%	[51]
Au-$BiVO_4$	Cr(VI) – 4-chlorophenol	4-CP – 0.1mM, Cr(VI) – 10mgL^{-1}, Time – 120 min	Cr(VI) – 83% 4-CP – 91%	[52]
N-TiO_2/rGO	Cr(VI) – Methylene Blue	Catalyst – 40mg, MB – 10mgL^{-1}, Cr(VI) – 1mgL^{-1}, pH – 7,	Cr(VI) – 97.84 MB – 97.92	[53]
Ag-$BiVO_4$	Cr(VI) – Ciprofloxacin	Catalyst – 20mg, Cr(VI) – 10mgL^{-1}, CIP – 10mgL^{-1},	CIP – 98.2% Cr(VI) – 95.63%	[13]
Bi_2S_3/rGO/$BiVO_4$	Cr(VI)-Bisphenol-A	Cr(VI) – 50ppm, BPA – 10ppm Time – 120 min	Cr(VI) – 100% BPA – 99.99%	[21]
CuNiFe LDH/C_3N_4	Cr(VI)+4-NP	Catalyst – 0.1gL^{-1}, Pollutant 10mgL^{-1}, pH-4	4-NP-19% Cr(VI)- 71.45%	This work
CuNiFe LDH/C_3N_4	Cr(VI)+2-CP	Catalyst – 0.1gL^{-1}, Pollutant 10mgL^{-1}, pH-5	2-CP-88.37% Cr(VI)- 40.94%	This work
CuNiFe LDH/C_3N_4	Cr(VI)+LEV	Catalyst – 0.1gL^{-1}, Pollutant 10mgL^{-1}, pH-4	LEV-68.66% Cr(VI)-77.56%	This work

3.5.4 Cr(VI) reduction under various conditions

The pH level of an aqueous solution stands as a paramount factor influencing the reduction of Cr(VI). Effect of pH on the photocatalytic activity of 1:2 (CuNiFe LDH/C_3N_4) was evaluated for photoreduction of Cr(VI) to Cr(III) at various pH (3,5, and 7). 1M NaOH and HNO_3 solutions were added to adjust the desired pH from pH 4.5. Regarding Cr(VI), pH directly effects the existing states of Cr(VI). In accordance with the ionic dissociation equilibrium, $Cr_2O_7^{2-}$ and $HCrO_4^-$ predominate at the pH range 2.0–6.0, and H_2CrO_4 appears at pH lower than 2.0, whereas only CrO_4^{2-} can exist stably in solution pH above 6.8 [15]. The adsorption capacity decreased in acidic pH in dark while the photocatalytic activity increased in the acidic pH. **Figure 3.11** shows Cr(VI) photoreduction outcome at different pH, where maximum photoreduction of Cr(VI) to Cr(III) was observed at pH 3 (88.4%). An increase in pH above 3 at 5 and 7 photoreduction of Cr(VI) decreases to 71.94% and 31.3% respectively.

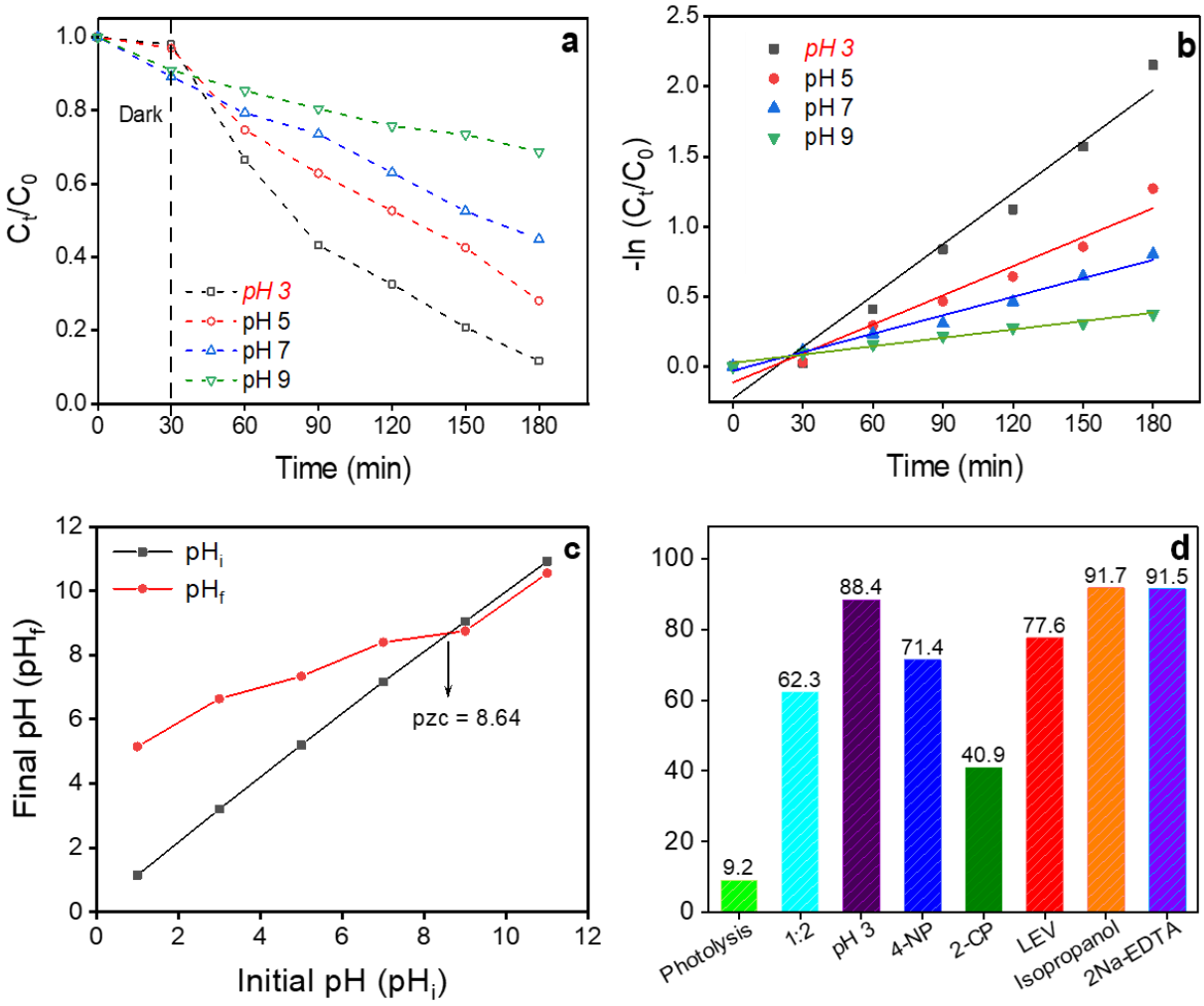

Figure 3.11: Cr(VI) removal at different pH (a) C_t/C_0, (b) $\ln(C_t/C_0)$, (c) point of zero charge of catalyst (1:2), and (d) chromium removal percentage under various conditions.

Apart from that the point of zero charge for the composite 1:2 was determined to be 8.64 which means that the catalyst surface below this pH the catalyst surface appears to be positive that promotes the adsorption of the oxyanions of Cr(VI) and results in the enhancement of the photoreduction of Cr(VI) to Cr(III) (**Eq. 3.1 and 3.2**). The reduction rate of Cr(VI) at pH 3 was the highest compared to others, with a regression of 0.96 (**Table 3.3**).

$$HCrO_4^- + 7H^+ + 3e^- \rightarrow Cr^{+3} + 4H_2O \quad 3.2$$

$$Cr_2O_7^{-2} + 14H^+ + 6e^- \rightarrow 2Cr^{+3} + 7H_2O \quad 3.3$$

Table 3.3: Kinetics of Cr(VI) reduction at different pH

pH	Reduction Rate K^{-1}	R^2	%age
3	$1.23x10^{-2} \pm 9.93x10^{-4}$	0.96	88.4
5	$6.92x10^{-3} \pm 6.21x10^{-4}$	0.95	71.9
7	$4.4x10^{-3} \pm 2.42x10^{-4}$	0.98	51.1
9	$1.99x10^{-3} \pm 1.17x10^{-4}$	0.98	31.3

3.5.5 Active species involved in pollutant removal

To identify the main active species in the reaction system, radicle trapping experiments were conducted by adding various scavengers into the photocatalytic system. As depicted in the **Figure 3.12 (a)**, 88.4% of the Cr(VI) underwent reduction in 180 min under sunlight irradiation at pH 3 over CuNiFe LDH/C_3N_4 1:2. Notably, the addition of 2Na EDTA and isopropanol (IP) elevated the photoreduction of Cr (VI) increases to 91.5% and 91.7% respectively. this enhancement can be attributed to the roles played by 2Na EDTA and isopropanol as h^+ and $OH^\cdot$ trapping agents in the reduction system, promoting charge separation, and enhancing the photoreduction of Cr(VI). Conversely, the presence of ascorbic acid (As) results in the partial suppression of Cr(VI) reduction (46.2%), indicating that $O_2^{\cdot-}$ also contributes to Cr(VI) reduction. Furthermore, the introduction of $AgNO_3$ led to a substantial decrease in Cr(VI) reduction to 22.4% from the initial 88.4%, suggesting a crucial role played by electrons in the reduction of the Cr(VI). Consequently, it can be concluded that $O_2^{\cdot-}$ and e^- are the predominant species in the Cr(VI) reduction over 1:2 (CuNiFe LDH/C_3N_4).

For 4-NP, the presence of IP and 2Na-EDTA led to a decrease in 4-NP degradation to 39.57% and 33.69%, respectively, signifying the involvement of the $OH^\cdot$ and h^+ play a significant role. Similarly, the removal rate decreased from 59.15% to 22.43% in the presence

of $AgNO_3$, indicating that e^- are the active species involved in the degradation of the 4-NP. Nevertheless, there was also about 17.79% efficiency loss when ascorbic acid was added (scavenger of superoxide radicle). This suggests that all the active species are somehow implicated in the degradation of 4-NP, but electrons have a more pronounced effect which may be the reason for the decreased removal efficiency of the 4-NP in the binary system with Cr(VI) as compared to the one in the absence of Cr(VI).

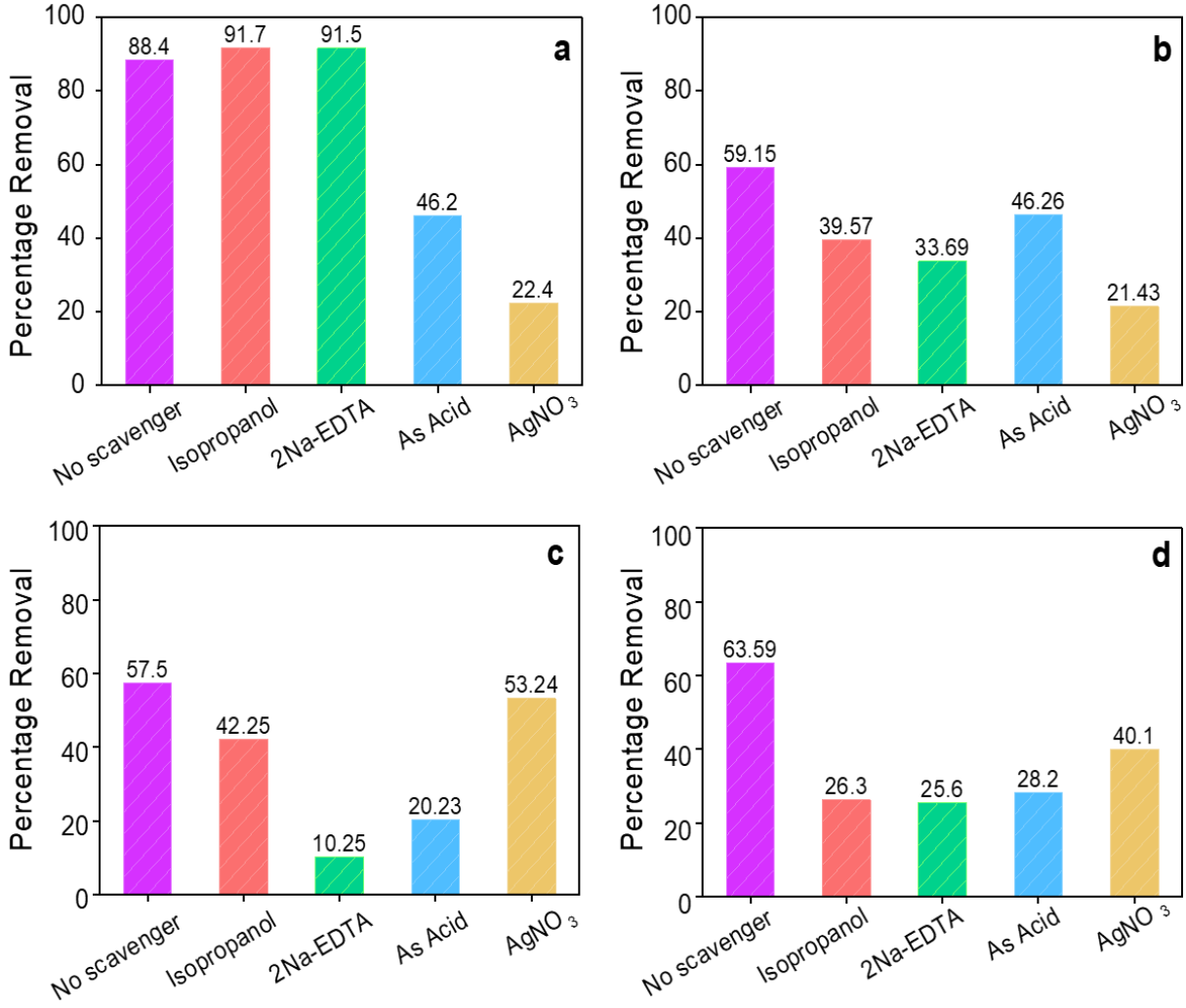

Figure 3.12: Effect of different scavengers on (a) Cr(VI) reduction, (b) 4-NP, (c) 2-CP, and (d) LEV degradation over 1:2. (Experimental conditions: catalyst dose – 0.1g/L, pollutant concentration – 10 mg/L)

In the case of 2-chlorophenol, $AgNO_3$ resulted in only about a 4.66% decrease in the 2-CP degradation, indicating that electrons are not the active species involved in 2-CP degradation. On the contrary, in the presence of IP, the degradation of 2-CP decreased from 57.9% to 42.25%. However, in the presence of ascorbic acid and 2Na-EDTA, the degradation of 2-CP decreased by 37.67% and 47.65% from 57.9%, respectively demonstrating that $O_2^{\cdot-}$ and h^+

are the active species involved in the degradation of 2-CP. This result may explain the decrease in the reduction of Cr(VI) in the presence of 2-CP, as $O_2^{\cdot-}$ radicles significantly reduce Cr(VI) and on the other hand the active trapping of the electrons by Cr(VI) may result in the free h^+, which may have led to the increased degradation of 2-CP in the binary system as compared to the single system.

For levofloxacin, in the presence of $AgNO_3$ the degradation of LEV decreased to 40.1% from 63.1%. When isopropanol, 2Na-EDTA, and ascorbic acid were added to the photocatalytic reaction system, the removal of LEV decreased to 26.3%, 25.6%, and 28.2% respectively, suggesting that $OH^{\cdot}$, holes, and $O_2^{\cdot-}$ are active species involved in the LEV degradation.

3.5.6 Proposed degradation pathway for organics

The **Figure 3.13** illustrates the potential pathway for the photocatalytic degradation of 4-nitrophenol. The hydroxyl group attach to the benzene ring serves as an electron donor, facilitating the electrophilic attack of $OH^{\cdot}$ on ortho position. This leads to the creation of 4-nitrocatechol. The nitro group of 4-nitrocatechol is then eliminated, resulting in the formation of hydro-quinol. When hydro-quinol reacts with super oxide radicle, it generates 2-hydroxy-1, 4-benzoqinone.

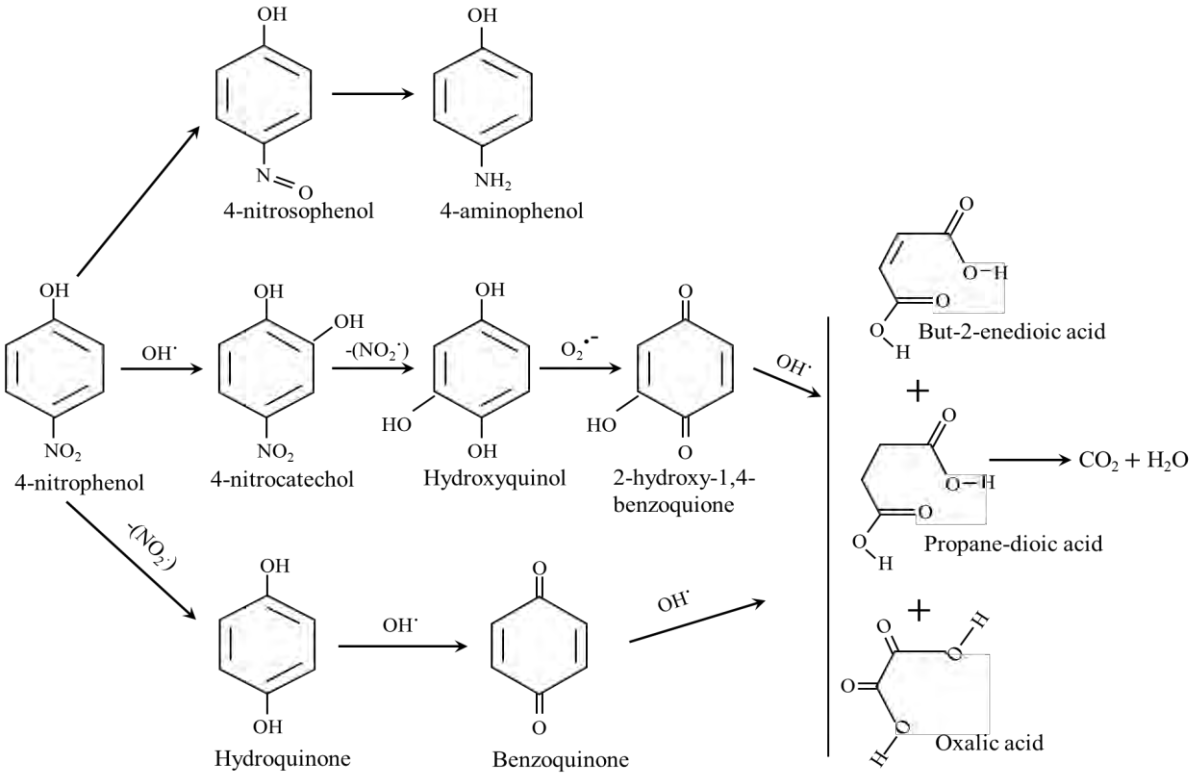

Figure 3.13: Illustration of the pathway for 4-NP photocatalytic degradation over 1:2.

An alternative degradation pathway involves the detachment of nitro group from 4-nitrophenol, yielding hydroquinone. Hydroquinone can then react with hydroxyl radicle to produce benzoquinone, establishing an oxidation pathway. Both benzoquinone and 2-hydroxy-1, 4-benzoquinone, when subjected to further oxidation, can yield by-products like oxalic acid, but-2-enedioic acid and propane-dioic acid. Upon complete mineralization, these by-products will transform to CO_2 and H_2O. Conversely, the reduction pathway results in the generation of 4-aminophenol through intermediate compound, 4-nitrosophenol [54–56].

The **Figure 3.14** illustrates the potential degradation pathway for 2-chlorophenol through oxidation using CuNiFe LDH/C_3N_4. Initially, 2-CP undergoes transformation into hydroxy hydroquinone due to attack on the ortho and para-positions, resulting in the removal of the halogen group [57]. Following this, the elimination of the hydroxyl group leads to the formation of catechol or hydroquinone (absorption peak near 260nm). Subsequently, these intermediates progress, ultimately yielding phenol [58]. Phenol undergoes further oxidation, giving rise to maleic acid or formic acid, eventually leading to the formation of acetic acid. Finally, acetic acid is converted into CO_2 and H_2O, completing the degradation pathway [59].

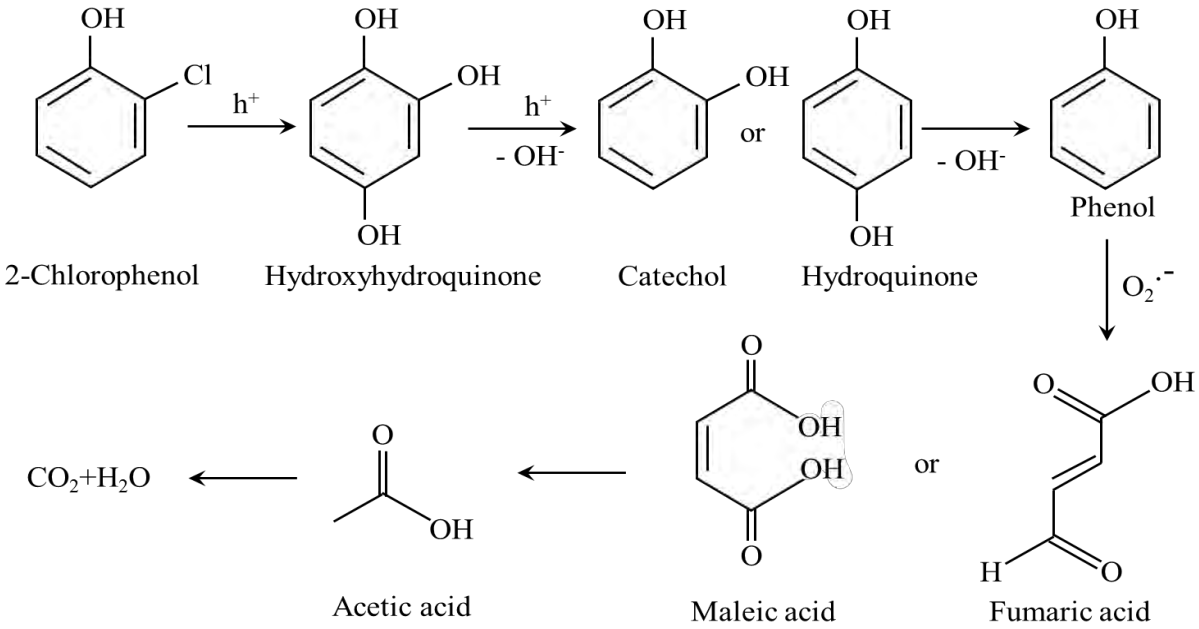

Figure 3.14: Schematic pathway for 2-CP photocatalytic degradation over 1:2.

Levofloxacin triggers a decarboxylation reaction within the methyl-morpholine group. The subsequent intermediate undergoes further degradation on the N-methyl piperazine ring, leading to oxidation and the creation of a stable intermediate [60]. Later, the intermediate compound undergoes de-alkylation, resulting in the formation of an intermediate that loses

$C_3O_2NH_4$ [61]. Furthermore, this intermediate may undergo additional processes such as defluorination and hydroxylation, continuing breakdown into smaller organic fragments. Ultimately, this sequence concludes through production of mineralization products [62].

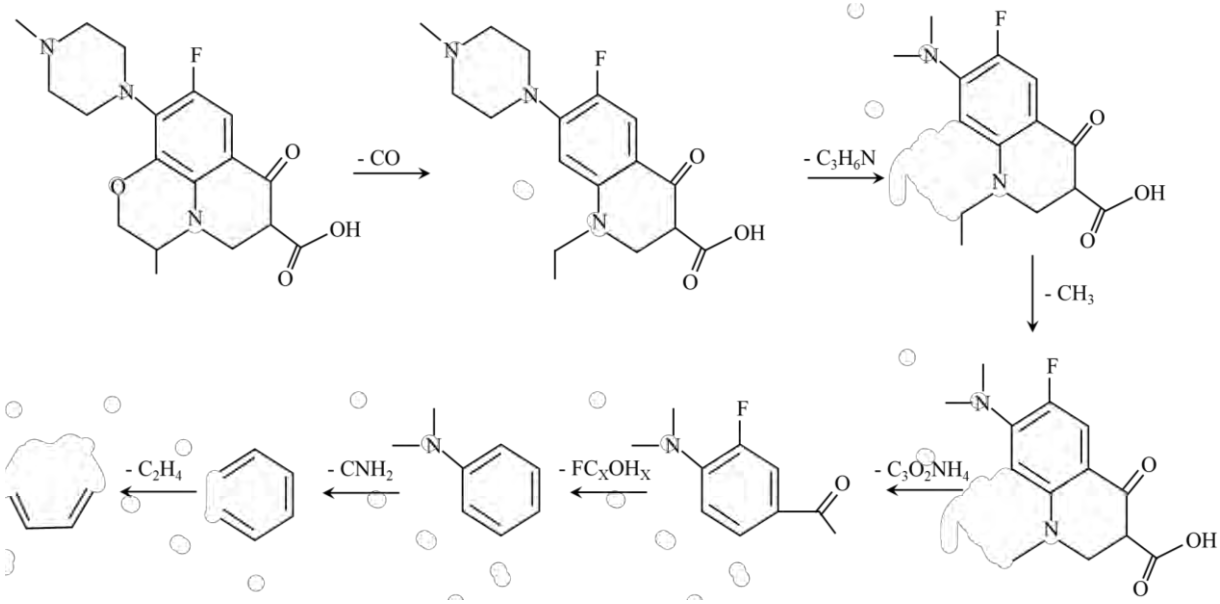

Figure 3.15: Step-by-step photocatalytic fragmentation of LEV over 1:2.

3.5.7 Mechanism study of pollutant removal

The potential mechanism underlying the reduction of Cr(VI) and degradation of organic compounds primarily involves processes such as electron capture and conversion of transition metal **Figure 3.16**. Initially, the Cr(VI) and organic compounds come into contact and are adsorbed on the surface of the CuNiFe LDH/C_3N_4. The layered structure of the CuNiFe LDH, along with the hydroxyl groups on the hydrotalcite structure, synergistically contributes to the transformation of pollutants. During photocatalytic activity, pollutants approach the edges and encounter the catalytic sites of the brucite-like sheets. The well-order layered structure of CuNiFe LDH may provide ample surface area for the reaction to take place. Additionally, the hydroxyl group on the sheets make the CuNiFe LDH/C_3N_4 catalyst hydrophilic, promoting the contact of the organic compounds with the reaction sites. Under sunlight, electrons from the valance band (VB) of the C_3N_4 move toward the conduction band (CB), creating corresponding holes in the VB. Subsequently, electrons in the CB of the C_3N_4 move toward CuNiFe LDH through the closely contacted interfaces. The metal-oxo-metal bridges and highly dispersed MO_6 octahedra facilitate the electron transfer from Ni^{+3}, Fe^{+3}, and Cu^{+2} to Ni^{+2}, Fe^{+2}, and Cu^{+}, driven by the electron from the C_3N_4. In this way, the photogenerated

electron-holes in the C_3N_4 will be separated effectively. Following this, holes can react with the hydroxyl group to form $OH^{\cdot}$.

$$CuNiFe\ LDH/C_3N_4 + Pollutant \rightarrow CuNiFe\ LDH/C_3N_4 - Pollutant \quad 3.4$$

$$C_3N_4 + hv \rightarrow h^+_{VB} + e^-_{CB} \quad 3.5$$

$$h^+ + H_2O \rightarrow OH^{\cdot} + H^+ \quad 3.6$$

$$OH^{\cdot} + OH^{\cdot} \rightarrow H_2O_2 \quad 3.7$$

$$C_3N_4(e^-) + O_2 \rightarrow O_2^{\cdot -} \quad 3.8$$

$$C_3N_4(e^-) + Cu^{+2} \rightarrow Cu^+ \quad 3.9$$

$$C_3N_4(e^-) + Ni^{+3} \rightarrow Ni^{+2} \quad 3.10$$

$$C_3N_4(e^-) + Fe^{+3} \rightarrow Fe^{+2} \quad 3.11$$

Moreover, Ni^{+2}, Fe^{+2}/Fe^{+3}, and Cu^+ present at the surface of CuNiFe LDH/C_3N_4 can accelerate the degradation of the organic compounds by producing active radicles (superoxide and hydroxyl radicle) and Ni^{+3}, Fe^{+3}/Fe^{+2}, and Cu^{+2} in the process. This cycle of the Ni^{+3}/Ni^{+2}, Fe^{+3}/Fe^{+2}, Cu^{+2}/Cu^+ continues, generating active species continuously. Meanwhile, the O_2 can also be converted to the $O_2^{\cdot -}$. These active species can react with the organic pollutants, producing intermediates and consequently the CO_2 and H_2O while Cr(VI) will be reduced to Cr(III).

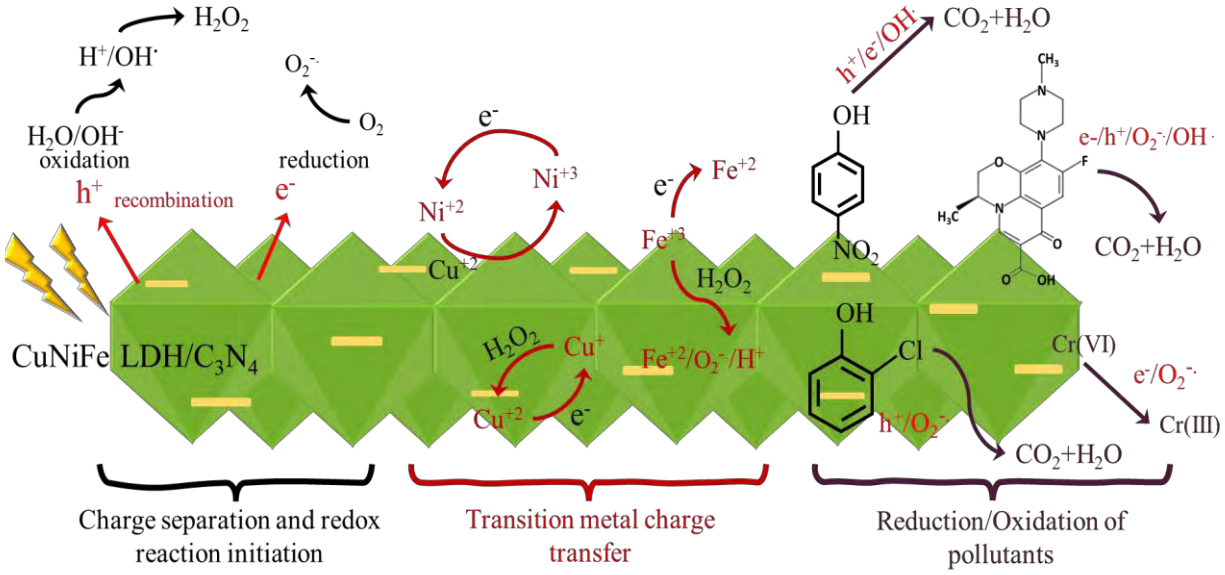

Figure 3.16: Suggested photocatalytic mechanism of pollutants removal over 1:2.

$$Ni^{+2} + Cu^{+2} \rightarrow Ni^{+3} + Cu^+ \quad 3.12$$

$$Cu^+ + H_2O_2 \rightarrow Cu^{+2} + OH^- + OH^{\cdot} \quad 3.13$$

$$Fe^{+3} + H_2O_2 \rightarrow Fe^{+2} + O_2^{\cdot -} + 2H^+ \quad 3.14$$

$$Fe^{+2} + H_2O_2 \rightarrow Fe^{+3} + OH^- + OH^{\cdot} \quad 3.15$$

$$Fe^{+2} + Ni^{+3} \rightarrow Fe^{+3} + Ni^{+2} \quad 3.16$$

$$C_3N_4(e^-) + HCrO_4^- \rightarrow Cr^{+3} \quad 3.17$$

$$C_3N_4(e^-) + Cr_2O_7^{-2} \rightarrow Cr^{+3} \quad 3.18$$

$$Cr(VI) + e^-/O_2^- \rightarrow Cr(III) \quad 3.19$$

$$C_6H_5ClO + O_2^-/h^+ \rightarrow \text{intermediate products} \rightarrow H_2O + CO_2 \quad 3.20$$

$$C_6H_5NO_3 + e^-/h^+/OH^\cdot \rightarrow \text{intermediate products} \rightarrow H_2O + CO_2 \quad 3.21$$

$$LEV + e^-/h^+/OH^\cdot/O_2^- \rightarrow \text{intermediate products} \rightarrow H_2O + CO_2 \quad 3.22$$

3.6 Stability of photocatalyst

Reusability and stability are important factors for the assessment of the practical application of the materials. The performance of the reusability of 1:2 CuNiFe LDH/C_3N_4 nanosheets was evaluated for Cr(VI) reduction as shown in Figure. After 4 runs the photoreduction of the Cr(VI) decreased 15% from 88.4% to 73.15%. that may be due to the catalyst loading during charging and recharging of 1:2 CuNiFe LDH/C_3N_4 nanosheets or due to the transition metal leaching during photocatalysis confirmed through ICP-OES (0.1% leaching noticed after 4 cycles). This confirms that the 1:2 CuNiFe LDH/C_3N_4 nanosheets is stable and reusable.

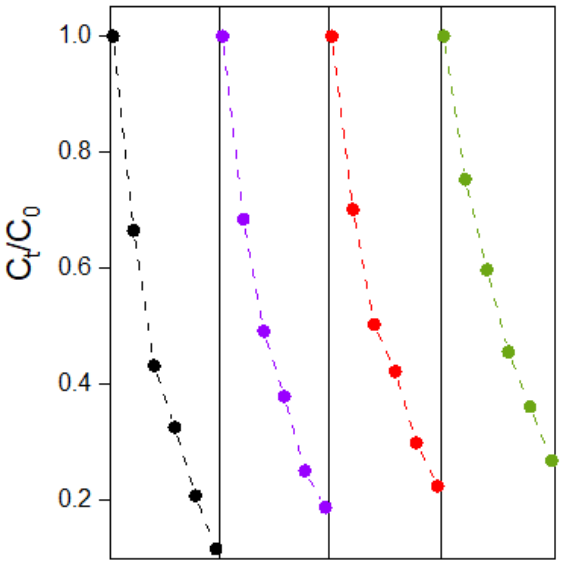

Figure 3.17: Cr(VI) photoreduction in four consecutive runs using CuNiFe LDH/C_3N_4 composite.

CONCLUSION

In summary, various CuNiFe LDH/C_3N_4 composites with different ratios were successfully synthesized. The investigation revealed that the layered structure of the CuNiFe LDH enhances pollutant binding and promotes charge separation. PL studies demonstrated the decreased electron-hole recombination, with the optimal working ratio identified as 1:2 (CuNiFe LDH/C_3N_4). The CuNiFe LDH/C_3N_4 was then assessed for its efficacy for simultaneous photocatalytic reduction of Cr(VI) and organic compounds 4-NP, 2-CP, and LEV. In the presence of 4-NP and LEV, an increased photoreduction of Cr(VI) was observed, attributed to the Cr(VI) acting as an active electron acceptor. Conversely, 2-CP resulted in decreased Cr(VI) reduction due its electron-donating and accepting effect. Organic compound degradation was also affected, with 4-NP degradation decreasing, possibly due to electron with-drawl effect and while 2-CP and LEV degradation increases in the presence of Cr(VI). Active species involved in Cr(VI) photoreduction are $e^-/O_2^{\cdot-}$, 4-NP are $e^-/h^+/OH^{\cdot}$, 2-CP $h^+/O_2^{\cdot-}$, and LEV are $e^-/h^+/OH^{\cdot}/O_2^{\cdot-}$. Furthermore, possible degradation pathways were proposed followed by comprehensive mechanism for deeper understanding. Reusability studies demonstrated that CuNiFe LDH/C_3N_4 maintained stability over four runs in Cr(VI) reduction.

REFERENCES

[1] A. Azizullah, M. N. K. Khattak, P. Richter, D. P. Häder, *Environ. Int.* **2011**, *37*, 479–497.

[2] M. K. Daud, M. Nafees, S. Ali, M. Rizwan, R. A. Bajwa, M. B. Shakoor, M. U. Arshad, S. A. S. Chatha, F. Deeba, W. Murad, I. Malook, S. J. Zhu, *Biomed. Res. Int.* **2017**, *23*, 134526.

[3] F. F. A. Aziz, A. A. Jalil, N. S. Hassan, A. A. Fauzi, M. S. Azami, N. W. C. Jusoh, R. Jusoh, *Environ. Res.* **2022**, *209*, 112748.

[4] A. Yadav, A. Raj, D. Purchase, L. F. R. Ferreira, G. D. Saratale, R. N. Bharagava, *Chemosphere.* **2019**, *224*, 324–332.

[5] L. Li, J. He, Z. Gan, P. Yang, *Chemosphere.* **2021**, *272*, 345213.

[6] M. Bibi, J. Rashid, A. Iqbal, M. Xu, *Phys. Chem. Earth, Parts A/B/C.* **2023**, *130*, 103398.

[7] A. Alamgir, M. A. Khan, N. Fatima, S. U. Fatima, *Environ. Monit. Assess.* **2023**, *195*, 6246.

[8] R. Saha, R. Nandi, B. Saha, *J. Coord. Chem.* **2011**, *64*, 1782–1806.

[9] Z. hua Liu, Y. Kanjo, S. Mizutani, *Sci. Total Environ.* **2009**, *407*, 731–748.

[10] R. Ameta, M. S. Solanki, S. Benjamin, S. C. Ameta, *Advanced Oxidation Processes for Wastewater Treatment*, **2018**, 1st Ed, 135–175.

[11] R. Ahmad, Z. Ahmad, A. U. Khan, N. R. Mastoi, M. Aslam, J. Kim, *J. Environ. Chem. Eng.* **2016**, *4*, 4143–4164.

[12] N. Tian, H. Huang, Y. He, Y. Guo, T. Zhang, Y. Zhang, *Dalton Trans.* **2015**, *44*, 4297–4307.

[13] M. Z. Abid, A. Ilyas, K. Rafiq, A. Rauf, M. A. Nadeem, A. Waseem, E. Hussain, *Environ. Sci.* **2023**, *9*, 2238–2252.

[14] Q. Guo, G. Tang, W. Zhu, Y. Luo, X. Gao, *J. Environ. Sci.* **2021**, *101*, 351–360.

[15] W. Zhao, J. Li, B. Dai, Z. Cheng, J. Xu, K. Ma, L. Zhang, N. Sheng, G. Mao, H. Wu, K. Wei, D. Y. C. Leung, *J. Chem. Eng.* **2019**, *369*, 716–725.

[16] A. Chachvalvutikul, T. Luangwanta, S. Kaowphong, *J. Colloid Interface Sci.* **2021**, *603*, 738–757.

[17] Y. Yu, K. Wu, W. Xu, D. Chen, J. Fang, X. Zhu, J. Sun, Y. Liang, X. Hu, R. Li, Z. Fang, *J. Hazard. Mater.* **2021**, *404*, 124171.

[18] S. Patnaik, D. P. Sahoo, K. M. Parida, *J. Colloid Interface Sci.* **2020**, *560*, 519–535.

[19] G. Xie, H. Wang, Y. Zhou, Y. Du, C. Liang, L. Long, K. Lai, W. X. Li, X. Tan, Q. Jin, G. Qiu, D. Zhou, H. Huo, X. Hu, X. Xu, *J. Taiwan. Inst. Chem. Eng.* **2020**, *112*, 357–365.

[20] F. Chen, Q. Yang, Y. Wang, F. Yao, Y. Ma, X. Huang, X. Li, D. Wang, G. Zeng, H. Yu, *J. Chem. Eng.* **2018**, *348*, 157–170.

[21] Q. Liang, S. Ploychompoo, J. Chen, T. Zhou, H. Luo, *J. Chem. Eng.* **2020**, *384*, 123256.

[22] H. Dong, G. Zeng, L. Tang, C. Fan, C. Zhang, X. He, Y. He, *Water Res.* **2015**, *79*, 128–146.

[23] Z. Long, Q. Li, T. Wei, G. Zhang, Z. Ren, *J. Hazard. Mater.* **2020**, *395*, 122599.

[24] A. K. Pearce, T. R. Wilks, M. C. Arno, R. K. O'Reilly, *Nat. Rev. Chem.* **2020**, *5*, 21–45.

[25] M. Ismael, *J. Alloys Compd.* **2020**, *846*, 156446.

[26] Q. Liang, Z. Li, Z. H. Huang, F. Kang, Q. H. Yang, *Adv. Funct. Mater.* **2015**, *25*, 6885–6892.

[27] A. Sherryna, M. Tahir, *Int. J. Energy Res.* **2022**, *46*, 2093–2140.

[28] P. Bobde, A. K. Sharma, D. Panchal, A. Sharma, R. K. Patel, R. S. Dhodapkar, S. Pal, *Inter. J. Environ. Tech.* **2022**, *22*, 04007.

[29] Z. zhu Yang, C. Zhang, G. ming Zeng, X. fei Tan, D. lian Huang, J. wu Zhou, Q. zhen Fang, K. hua Yang, H. Wang, J. Wei, K. Nie, *Coord. Chem. Rev.* **2021**, *446*, 214103.

[30] Z. Z. Yang, C. Zhang, G. M. Zeng, X. F. Tan, H. Wang, D. L. Huang, K. H. Yang, J. J. Wei, C. Ma, K. Nie, *J. Mater. Chem. A Mater.* **2020**, *8*, 4141–4173.

[31] H. Zhang, L. chao Nengzi, Z. Wang, X. Zhang, B. Li, X. Cheng, *J. Hazard Mater.* **2020**, *383*, 121236.

[32] R. Rashid, I. Shafiq, P. Akhter, M. J. Iqbal, M. Hussain, *Environ. Sci. Pollut. Res.* **2021**, *28*, 9050–9066.

[33] F. Z. Janani, N. Taoufik, H. Khiar, W. Boumya, A. Elhalil, M. Sadiq, A. V. Puga, N. Barka, *Surf. Interfaces,* **2021**, *25*, 101263.

[34] J. Epp, Materials Characterization Using Nondestructive Evaluation (NDE) Methods **2016**, 81–124.

[35] A. A. Bunaciu, E. G. Udristioiu, H. Y. A. Enien, *Crit. Rev. Anal. Chem.* **2015**, 289-299.

[36] R. Ummaleti, W. Boumya, *Minerals***, 2019**, *12(2),* 205.

[37] A. V. Puga, J. Torrent, S. Arcozzi, *Character. Mater*, **2019**.

[38] A. Mohammed, A. Abdullah, *Inter. Hydra.* **2018**, 77–85.

[39] J. Torrent, V. Barrón, *Soil Anal,* **2015**, *5*, 367–385.

[40] P. Morozzi, B. Ballarin, S. Arcozzi, E. Brattich, F. Lucarelli, S. Nava, P. J. Gómez-Cascales, J. A. G. Orza, L. Tositti, *Atmos. Environ.* **2021**, *252*, 118297.

[41] F. Chen, F. Lucarelli, *Atmos. Environ.* **2022**. *252,* 118297.

[42] T. Aoki, *Character. Mater.* **2012**, 1–12.

[43] A. Sanchez-Hachair, A. Hofmann, *Mater. Res.* **2018**, 05002.

[44] U. Zahoor, M. I. Rameel, A. H. Javed, M. A. Khan, J. Y. Al-Humaidi, S. Iqbal, A. M. Aldawsari, A. Shah, *Int. J. Environ. Res.* **2022**, *16*, 1–14.

[45] L. L. Liu, F. Chen, J. H. Wu, W. W. Li, J. J. Chen, H. Q. Yu, *J. Mater. Chem. A Mater.* **2021**, *9*, 10933–10944.

[46] C. A. Antonyraj, S. Kannan, *Appl. Clay Sci.* **2011**, *53*, 297–304.

[47] N. Wen, Y. Su, W. Deng, H. Zhou, M. Hu, B. Zhao, *J. Chem. Eng.* **2022**, *438*, 135570.

[48] H. Wang, M. Jing, Y. Wu, W. Chen, Y. Ran, *J. Hazard Mater.* **2018**, *353*, 53–61.

[49] Y. Yu, D. Chen, W. Xu, J. Fang, J. Sun, Z. Liu, Y. Chen, Y. Liang, Z. Fang, *J. Hazard Mater.* **2021**, *416*, 126183.

[50] L. Fu, Z. Yan, Q. Zhao, H. Yang, *Adv. Mater. Interfaces* **2018**, *5*, 1801094.

[51] W. Xie, E. Pakdel, Y. Liang, D. Liu, L. Sun, X. Wang, *J. Photochem. Photobiol. A Chem.* **2020**, *389*, 112292.

[52] Y. Wei, Y. Zhang, W. Geng, H. Su, M. Long, *Appl. Catal. B Environ.* **2019**, *259*, 118084.

[53] M. Utami, S. Wang, M. M. Musawwa, T. E. Purbaningtias, M. Fitri, I. Yuspita, O. H. Abd-Elkader, K. K. Yadav, G. Munusamy-Ramanujam, D. Bang, S. W. Chang, B. Ravindran, *Chemosphere* **2023**, *332*, 138882.

[54] V. Yadav, P. Verma, H. Negi, R. K. Singh, V. K. Saini, *J. Mater. Res.* **2023**, *38*, 237–247.

[55] P. V. R. K. Ramacharyulu, S. J. Abbas, S. R. Sahoo, S. C. Ke, *Catal. Sci. Technol.* **2018**, *8*, 2825–2834.

[56] N. Verma, R. Ananthakrishnan, *ChemPhotoChem* **2021**, *5*, 545–558.

[57] S. Chaveanghong, T. Kobkeatthawin, J. Trakulmututa, T. Amornsakchai, P. Kajitvichyanukul, S. M. Smith, *RSC Adv.* **2023**, *13*, 17565–17574.

[58] M. M. Ba-Abbad, M. S. Takriff, A. A. H. Kadhum, A. B. Mohamad, A. Benamor, A. W. Mohammad, *Environ. Sci. Pollut. Res.* **2017**, *24*, 2804–2819.

[59] N. N. Rao, A. K. Dubey, S. Mohanty, P. Khare, R. Jain, S. N. Kaul, *J. Hazard. Mater.* **2003**, *101*, 301–314.

[60] M. I. Rameel, M. Wali, J. Y. Al-Humaidi, F. Liaqat, M. A. Khan, *Heliyon* **2023**, *9*, 20479.

[61] S. L. Prabavathi, K. Saravanakumar, C. M. Park, V. Muthuraj, *Sep. Purif. Technol.* **2021**, *257*, 117985.

[62] S. Sharma, A. Umar, S. K. Mehta, A. O. Ibhadon, S. K. Kansal, *New. J. Chem.* **2018**, *42*, 7445–7456.